




## Site Response Analysis of Anchorage, Alaska Using Generalized Inversions of Strong-Motion Data (2004–2019)

JOHN THORNLEY,<sup>1,2</sup>  JOHN DOUGLAS,<sup>1</sup> UTPAL DUTTA,<sup>3</sup> and ZHAOHUI YANG<sup>3</sup>

**Abstract**—Anchorage, Alaska, is located in one of the most active tectonic settings in the world. The city and region were significantly impacted by the  $M_W$  9.2 Great Alaska Earthquake in 1964, and they were recently shaken by a  $M_W$  7.1 event in 2018. The city was developed in an area underlain by complex soil deposits of varied geological origins and stiffnesses, with the deposits' thicknesses increasing east to west. Situated at the edge of the North American Plate, with the actively subducting Pacific Plate below, Anchorage is susceptible to both intraslab and interface earthquakes, along with crustal earthquakes. Strong-motion stations were installed across the city in an attempt to capture the variability in site response. Several previous studies have been performed to evaluate that variability but have not included larger magnitude events and have not benefited from the current density of instrumentation. The work presented here provides background information on the geology and tectonic setting of Anchorage and presents details related to the dataset and methods used to perform the site-response analysis. This study has collected strong-motion recordings from 35 surface stations across Anchorage for 95 events spanning from 2004 to 2019, including the  $M_W$  7.1 Anchorage Earthquake in 2018. The more than 1700 three-component recordings from those 95 events with moment magnitudes ranging from 4.5 to 7.1 were used to evaluate site response variability across the city. Using the Generalized Inversion Technique and a reference rock site, spectral amplifications were calculated and analyzed for frequencies between 0.25 and 10 Hz for each strong-motion station. The study results were used to develop contour maps at 1 Hz and 5 Hz, using logarithmic-band averages, to describe the variability of spectral amplifications at these two frequencies of interest. The results were also compared to geologic conditions across Anchorage, and the overlaying of different soil deposits can be seen to have an impact on the spectral amplification at the sites. The results of this study provide improvements on past microzonation studies and, using sensitivity analyses, offer support for the use of small and moderate earthquakes to evaluate spectral amplifications.

**Keywords:** Earthquake ground motions, Earthquake hazards, Site effects, Spectral amplification.

### 1. Introduction

Southcentral Alaska is one of the most seismically active regions of the world. It is located at the convergence of the Pacific and North American tectonic plates, which results in a variety of seismic sources, including deep subduction intraslab and interface earthquakes, as well as crustal earthquakes (Wesson et al., 2007). Southcentral Alaska also has approximately half of the state's population, primarily living and working in Anchorage. The 1964 Great Alaska Earthquake ( $M_W$  9.2), which is the second-largest earthquake recorded in modern history (USGS.gov, 2020), affected southcentral Alaska, including Anchorage, and resulted in significant ground failure. While Anchorage's population in the 1960s was approximately 44,000 (U.S. Bureau of the Census, 1963), the current population has grown to 291,000 (Census.gov, 2020); since the earthquake hazard has not reduced, the risk remains high.

The Anchorage area sits in a geologically complex area of southcentral Alaska. Mountain building at the edge of the subduction zone and episodic glaciation have affected the geology and created a basin of soft sediments composed of sands, gravels, and clay overlying a steeply dipping Tertiary rock (Combellick, 1999). An initial microzonation study was started in the 1990s by Biswas et al. (2003) within Anchorage, and several digital seismic strong-motion stations were installed across Anchorage to measure the variability of ground motions across the city (Biswas et al., 2004; Dutta et al., 2003; EERI,

<sup>1</sup> Department of Civil and Environmental Engineering (UK), University of Strathclyde, Glasgow, UK. E-mail: john\_thornley@golder.com

<sup>2</sup> Golder Associates Inc. (USA), Anchorage, USA.

<sup>3</sup> Department of Civil Engineering (USA), University of Alaska, Anchorage, USA.

2019; Franke et al., 2019; Martirosyan et al., 2002). Since then, several strong-motion stations have been added to the network by a variety of working groups. The network now consists of more than 30 surface strong-motion stations and a downhole array. Additionally, several buildings and bridges were instrumented to measure their structural response (e.g., Xiong & Yang, 2008; Yang et al., 2004).

This study presents the findings from the site response analysis of 35 surface strong-motion stations located in Anchorage, including the development of the database, methodology for performing the site response analysis for the selected stations, and a summary of the main results. This study represents a substantial improvement of the previous seismic microzonation studies for Anchorage, Alaska, as it uses data from more seismic stations representing various geological units and more and larger-amplitude strong-motion records than used in previous studies.

Microzonation studies like this consider the varied site response across Anchorage and allow the development of more resilient infrastructure that will suffer less damage and will recover more quickly after the next large earthquake. Anchorage serves a strategic community for a variety of services and operations such as the fifth busiest cargo airport in the world; United States military installations; and a deep-water port that receives 75% of the goods arriving in Alaska. Impacts on infrastructure due to earthquakes can be significant, and mitigation of the earthquake risk is critical to the continued operation of these facilities.

## 2. Tectonic Setting, Seismicity and Near-Surface Geology of Southcentral Alaska

Southcentral Alaska is on the North American Plate, with the Pacific Plate subducting below at a rate of 55 mm/yr (Haessler, 2008). The depth of the interface between the two plates ranges from 25 to 40 km in the region around Anchorage (Hayes et al., 2018; Wesson et al., 2007). Both intraslab and interface earthquakes occur in this region. The most notable interface earthquake was the 1964  $M_W$  9.2 Great Alaska Earthquake, which ruptured

approximately 800 km of the Alaska-Aleutian megathrust (Freymueller et al., 2008). An example of a notable recent intraslab earthquake is the 2018  $M_W$  7.1 Anchorage Earthquake, which caused extensive damage to infrastructure in southcentral Alaska (West et al., 2020). The 2018 Anchorage Earthquake occurred at a depth of more than 40 km, representing a common observation that the subduction-zone earthquakes are quite deep in this region.

In addition to the subduction-zone earthquakes, additional seismic sources include shallow crustal faults and folds (presented in Fig. 1 of Thornley et al., 2021a) in the Cook Inlet west and southwest of Anchorage and those in the northwest of Anchorage, including the Castle Mountain fault (Koehler et al., 2012). While the Cook Inlet crustal faults and folds are not likely to generate earthquakes of similar magnitude to the interface and intraslab earthquakes, they are much shallower than the subduction events and can potentially cause significant damage to the built environment. The Castle Mountain fault complex, which includes the Lake Clark fault to the west, can produce earthquakes up to  $M_W$  7.1–7.5 (Haessler et al., 2002; Wesson et al., 2007).

The geology of Anchorage varies significantly from east to west (Fig. 1). The Chugach Mountains, an accreted and lightly metamorphosed greywacke, border the city to the east (Wilson et al., 2012). Glacial valleys trend through the mountains in a northwest orientation and glacial outwash materials are found at the base of the mountains. The Chugach Mountains dip steeply to the northwest, and the sedimentary soil thickness reaches a depth of 500 m overlying Tertiary sandstone at the western edge of the city (Combellick, 1999; Glass, 1988; Schmoll & Barnwell, 1984). The soil overlying bedrock consists of a range of soils, from dense glacial outwash and till with shear wave velocities greater than 1,000 m/s (Thornley et al., 2019) to soft, cohesive lacustrine soil with shear wave velocities of 150 m/s (Updike et al., 1988). Erosional events related to several glaciation events have affected the thickness and lateral deposition of these different soils (Combellick, 1999; Ulery & Updike, 1983). Such marine transgressions and glacial advance and retreat cause soil heterogeneities, and hence significant variability in the

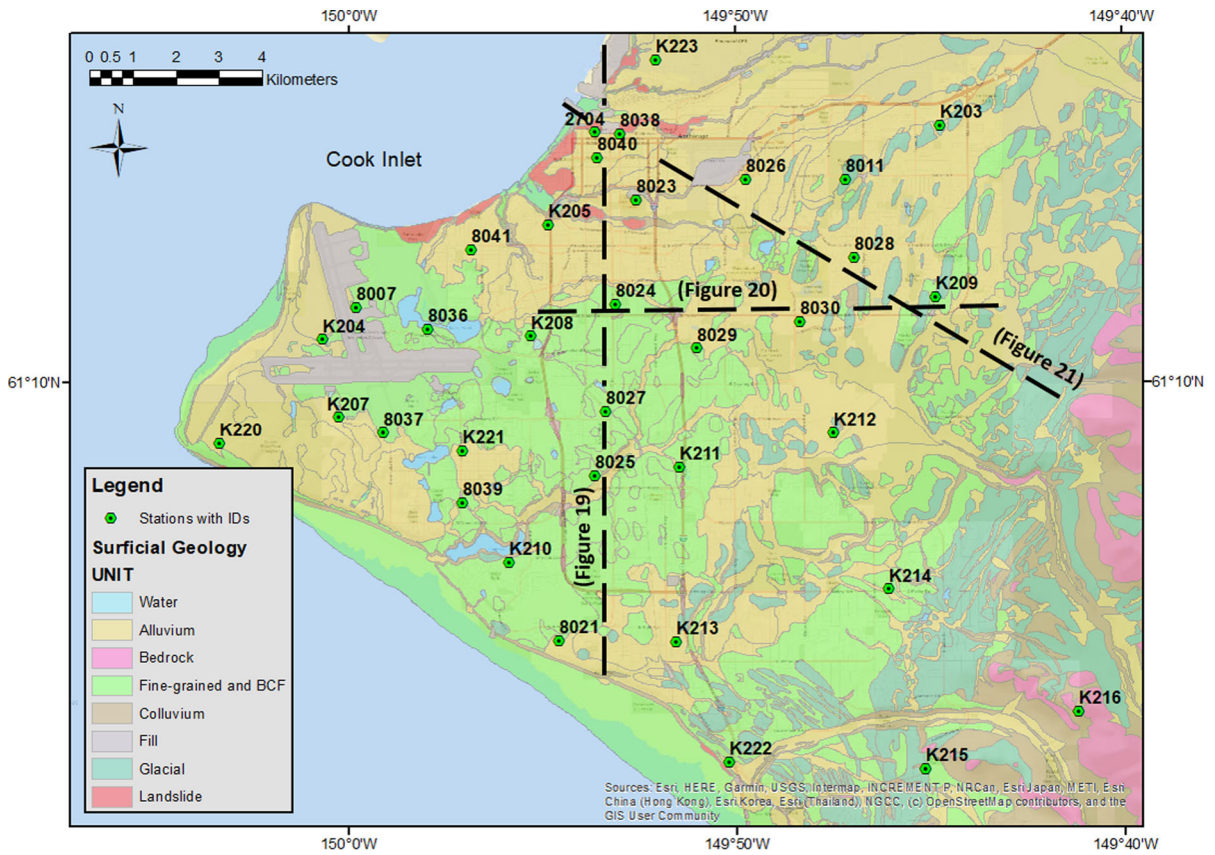


Figure 1

Strong motion station locations in Anchorage, Alaska. The generalized surficial geology is provided in the background to show variability, along with cross-section locations (dashed black lines) with figure references described in subsequent sections

amplification of earthquake ground motions across Anchorage.

The surficial geology consists of several soil units, including dense glacial till, glacial outwash, alluvium, and lacustrine deposits (Schmoll & Dobrovolny, 1972). The dense glacial till extends across the city and is near the surface in the eastern portion of the city. In the northern part of the city, the glacial till is overlain by glacial outwash deposits. Overlying the glacial till in the central and western portions of the city are alluvial deposits of varying thickness. The main soil unit found to have a significant impact on ground motions and site response is the Bootlegger Cove Formation (BCF). The BCF has several facies, including sand, silt, and clay. One of the sensitive clay facies is responsible for the significant ground failures in the 1964 Great Alaska

Earthquake. The BCF is generally centered in the middle portion of the city, with the more sensitive clay facies located in the north and overlain by silt and sand in the south (Combellick, 1999; Updike & Ulery, 1986).

### 3. Anchorage Strong Motion Network and Strong Motion Data Used

At the time of the Great Alaska Earthquake, March 27, 1964, there were only two seismograph stations located within Alaska. These included one station in Sitka and one in Fairbanks. The Sitka Observatory was established in 1904, located 950 km southeast of Anchorage. In Fairbanks, the University of Alaska College Observatory was established in

1935. Fairbanks was the closer of the two stations to Anchorage, but it was over 400 km north of Anchorage. As a result, no local strong-motion records of the Great Alaska Earthquake exist (Hansen, 1965). In the years following this monumental event, numerous seismograph stations were installed and operated by the U.S. Geological Survey, U.S. Army Corps of Engineers, and others. By 1976 there were more than 40 stations across Alaska, including five stations in Anchorage (Procella, 1979).

As mentioned previously, in 1993, an effort was launched to provide a further understanding of the variability in Anchorage's seismicity through a multi-agency seismic microzonation study. Twenty-two digital surface strong-motion stations were established across the Anchorage metropolitan area (Biswas et al., 2004). Several studies have been performed using data from those stations, including those by Biswas et al. (2003) and Dutta et al. (2003). In comparison to the current work, these previous studies were achieved with fewer stations (Alaska Science and Technology Foundation stations identified as K2XX Stations) and strong-motion records of small ( $M_W$  3.3) to moderate earthquakes ( $M_W$  6.5). The recent growth of the network, including the stations of the USGS National Strong Motion Program (NSMP Stations) and the Delaney Park Downhole Array (DPDA), dating from 2004, allows better characterization of the variability in response due to Anchorage's complex geology. In the early 2000s, the strong-motion data from the K2XX and NSMP stations started being collected at a single location, the Alaska Earthquake Center (AEC). Figure 1 presents the stations included in this analysis, and the latitude and longitude of each of the stations are included in "Appendix A". This study uses ground motions recorded by this network to update and refine the microzonation work performed previously by others.

The strong-motion data used in this study are of earthquakes between 2004 and 2019, including the November 30, 2018  $M_W$  7.1 Anchorage Earthquake, which was recorded by 28 of the stations used in this study. Except for the DPDA data, the strong-motion records were primarily provided by the AEC. The AEC provided earthquake date, time, hypocentral location, and magnitude for the strong-motion

records. The DPDA data were downloaded from the University of California, Santa Barbara (<http://www.nees.ucsb.edu/>), while the data from the  $M_W$  7.1 Anchorage Earthquake and larger aftershocks were downloaded from IRIS (<https://www.iris.edu/hq/>). The study includes recorded earthquakes with local magnitudes ( $M_L$ ) greater than 4.5 and at epicentral distances less than 300 km. The cut-off distance of 300 km was chosen to include the  $M_W$  7.1 Iniskin Earthquake (January 24, 2016). A summary of the events used in this study is provided in "Appendix B".

The database included records that were characterized in local magnitude ( $M_L$ ), body-wave magnitude ( $m_b$ ), and moment magnitude ( $M_W$ ) scales. The magnitude scales were unified to  $M_W$ . Magnitudes in  $m_b$  and  $M_L$  scales were considered equal because of their relatively low magnitudes (typically below  $M$  6) and based on research by Ruppert and Hansen (2010). These magnitudes were then converted to the  $M_W$  scale using the correlation by Dutta et al. (2003) which was developed for southcentral Alaska (Eq. 1). Larger magnitude events in the database were characterized in the  $M_W$  scale and did not require conversion.

$$M_W = (0.855 \pm 0.04)M_L + (0.58 \pm 0.17) \quad (1)$$

### 3.1. Time History Processing

The strong-motion stations located across Anchorage primarily consist of Kinometrics sensors. Many of these stations started with Altus K2 sensors and most have been upgraded over time to Basalt sensors. Most stations record at a sampling rate of 200 Hz, and, with the exception of the DPDA, all of the stations used in the study provide continuous data and are monitored by the AEC. The data used in this study was in the SAC format with a typical acceleration time history record length of around 300 s, including, in most cases, at least 20 s of pre-event (noise) data. The Seismic Analysis Code (SAC) (Goldstein & Snoke, 2005) was selected to process the strong-motion data.

The acceleration data was processed by removing the mean and trend using a least-squares fit (Goldstein & Snoke, 2005). The SAC function that



removes glitches or irregularities in the records caused during data acquisition was also applied, where glitches refer to artificial spikes caused by samples that are orders of magnitude higher than the surrounding data (Goldstein et al., 2003; Helffrich et al., 2013). A fourth-order Butterworth bandpass filter was applied to the acceleration time histories, and various high and low-frequency limits were evaluated. Methods presented by Akkar and Bommer (2006) were utilized to verify the low-frequency (long-period) filter cut-off selection. Considerations for high-frequency (short-period) cutoff filters used the methods described by Douglas and Boore (2011).

The frequency range of interest for this engineering study is between 0.25 and 10 Hz, which matches the range of fundamental frequencies of structures within the city. Visual screening of records was performed to evaluate a reasonable bandwidth filter that could be applied to most records and maintain the frequency range of interest for this study. The quality of the recordings was evaluated using the signal-to-noise ratio (SNR), where the Fourier amplitude spectrum of the recorded signal and the pre-event noise were calculated. An example time history and its signal and noise Fourier amplitude spectra are shown in Fig. 2. Each record was evaluated and those with a SNR of less than 3 within the frequency range of interest (0.25–10 Hz) after filtering between 0.1 and 30 Hz were excluded from this study. This practice reduced the number of available three-component records to 1727 from 95 events, which is 70% of the original dataset. The unused records were generally from small deep (> 40 km) subduction earthquakes and were typically more than 100 km from Anchorage, which resulted in a SNR less than 3 within the frequency range of interest.

Surface waves can increase the uncertainty in the results of site amplification studies like this one because they have different characteristics to S waves (Bonilla et al., 1997; Oth et al., 2009). To reduce the impact of surface waves on the results, a window of 10 s was used starting at the S-wave arrival. The 10-s S-wave window was selected based on a visual evaluation of the records to capture the high-amplitude portion of the records. With the selection of a general window, there is a possibility of including some of the surface waves of some records,

especially for distant lower magnitude events. Varying the window length between 5 and 15 s did not, however, have an observable effect on site amplification when only the lower magnitude events were included. The noise window was selected as the portion of the record before the P-wave arrival and was generally longer than 10 s, depending on the record. The P- and S-wave arrival times were chosen by visual inspection of the three-component records used during the time-history processing. An example of a horizontal acceleration time history with noise and S-wave windows is presented in Fig. 2. It should be noted that large low-frequency site responses can be associated with surface waves, particularly in sedimentary basins such as Anchorage, and hence the focus of this study on only S waves may be underestimating the low frequency response at some sites.

Thornley et al. (2021a) presents the distribution of earthquakes used in this study and identifies the crustal, interface, and intraslab events, as determined by using the depth and geometry of the subduction zone defined by Hayes et al. (2018). Figure 3 presents the epicentral distance versus the magnitude of the events in the database. Note that the DPDA Station 8040, with latitude and longitude given in “Appendix A”, was chosen as the point in Anchorage used to define a general epicentral distance from the city, although site-specific distances were used in the analyses. The hypocentral distance by azimuth is presented in Fig. 4 showing a concentration of earthquake events in two azimuthal ranges, 225°–250° and 330°–360°. A sensitivity analysis is presented below, evaluating the azimuth effects on the results of this study. The database consists primarily of  $M_w$  4.5–5.5 events (Fig. 5a). Additional information describing the distribution of data across epicentral distance, depth, and azimuth from Anchorage is presented in Fig. 5b–d. The station with the most recordings (70 in total) was K213 and the station with the fewest (only 6) was K207. The 35 stations had an average of 48 records each. The number of events recorded at each station and used in this study is presented in Fig. 6.

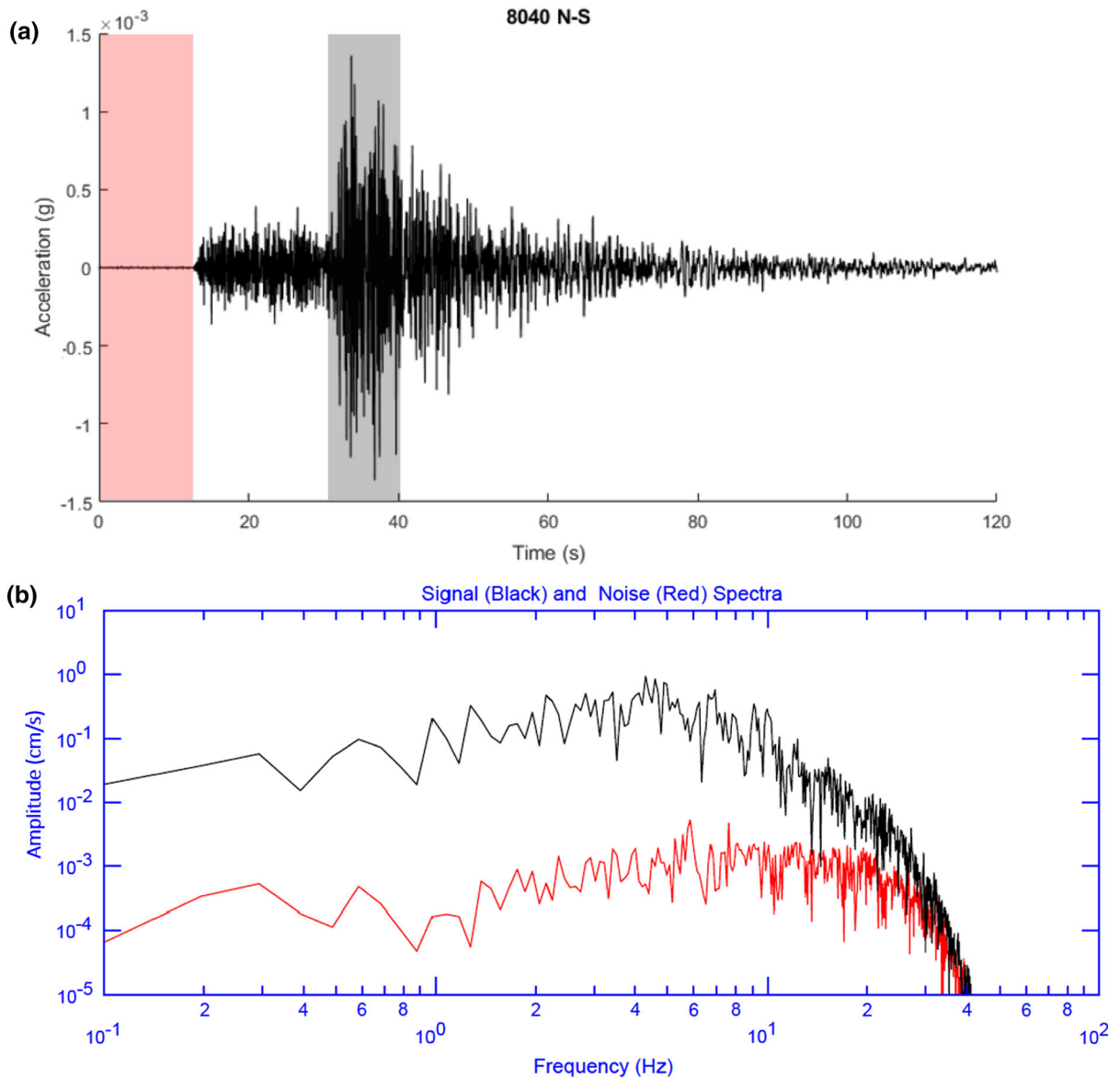


Figure 2

Example time history plot **a.** where the pre-event noise window is indicated in red and the S-wave window is in grey and **b.** the Fourier amplitude spectrum of the filtered signal (in black) and the noise (in red)

#### 4. Site Response Evaluation

Not all events were recorded at every station either due to a low SNR or because the station was not functioning at the time. To include as many strong-motion stations as possible the Generalized Inversion Technique (GIT) was used to evaluate the spectral amplifications (where it is assumed that

spectral amplifications provide an indicator of site response) for a site (Andrews, 1986; Castro et al., 2004; Priolo et al., 2019). The GIT methodology allows for gaps in the completeness of the dataset, providing a way to incorporate as many sites as practicable.

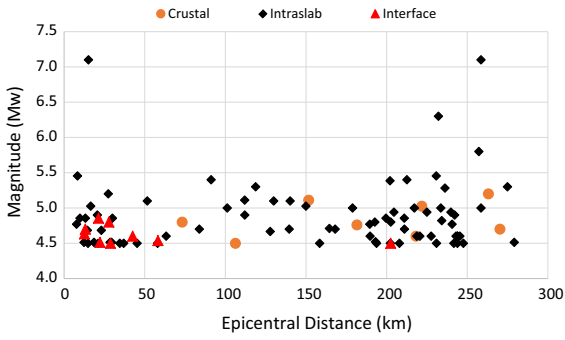


Figure 3  
Epicentral distance versus magnitude with crustal, intraslab, and interface events identified

#### 4.1. GIT Background Information

The use of GIT in site response analysis has become common since the original article by Andrews (1986), e.g., Parolai et al. (2000), Dutta et al. (2003), Oth et al. (2009), Bindi et al. (2017), and Laurenzano et al. (2019). Constraints applied to the source, path, and site terms in the spectral domain allows the indeterminate matrix to be solved. One constraint, such as the selection of a reference site, provides a simple way to constrain the matrix within microzonation studies (Klin et al., 2018). The main assumption of GIT is that in the frequency domain, the logarithmic value of the observed amplitude

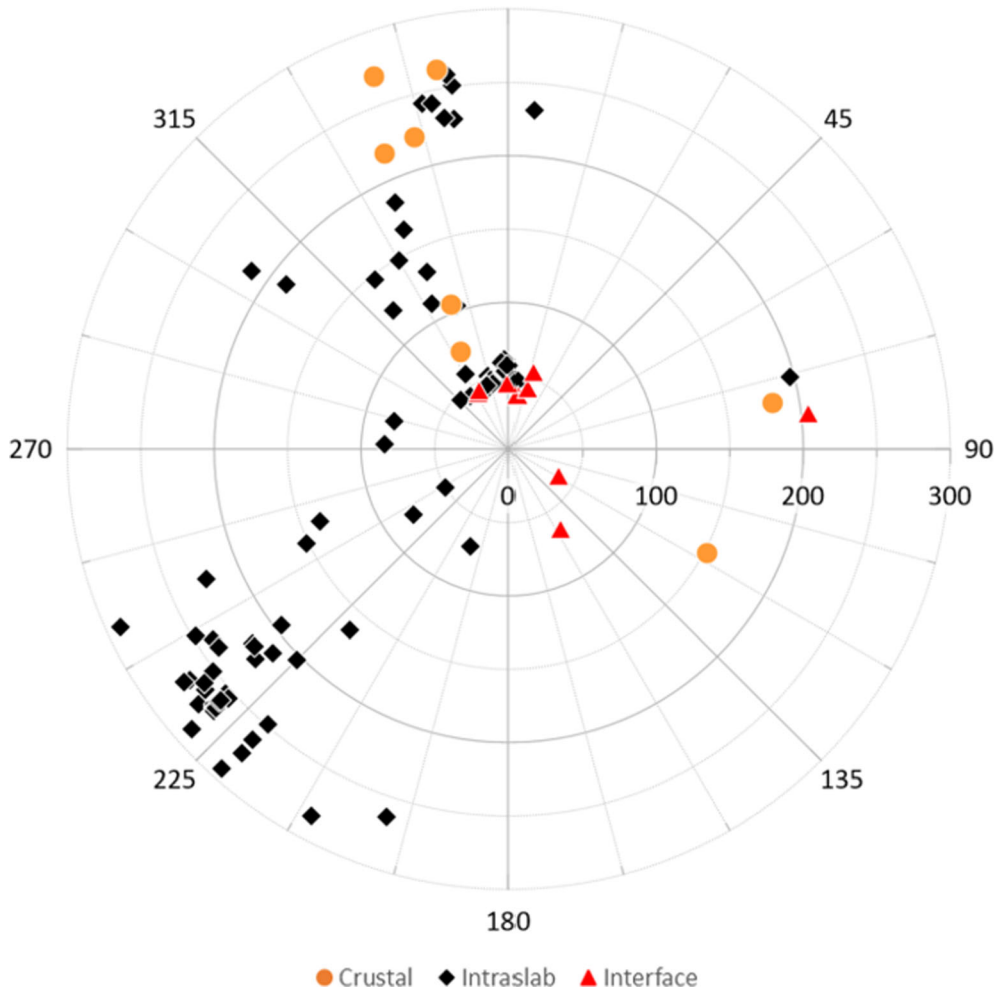


Figure 4  
Hypocentral distance, in kilometers, and azimuth relationship for crustal, intraslab, and interface events

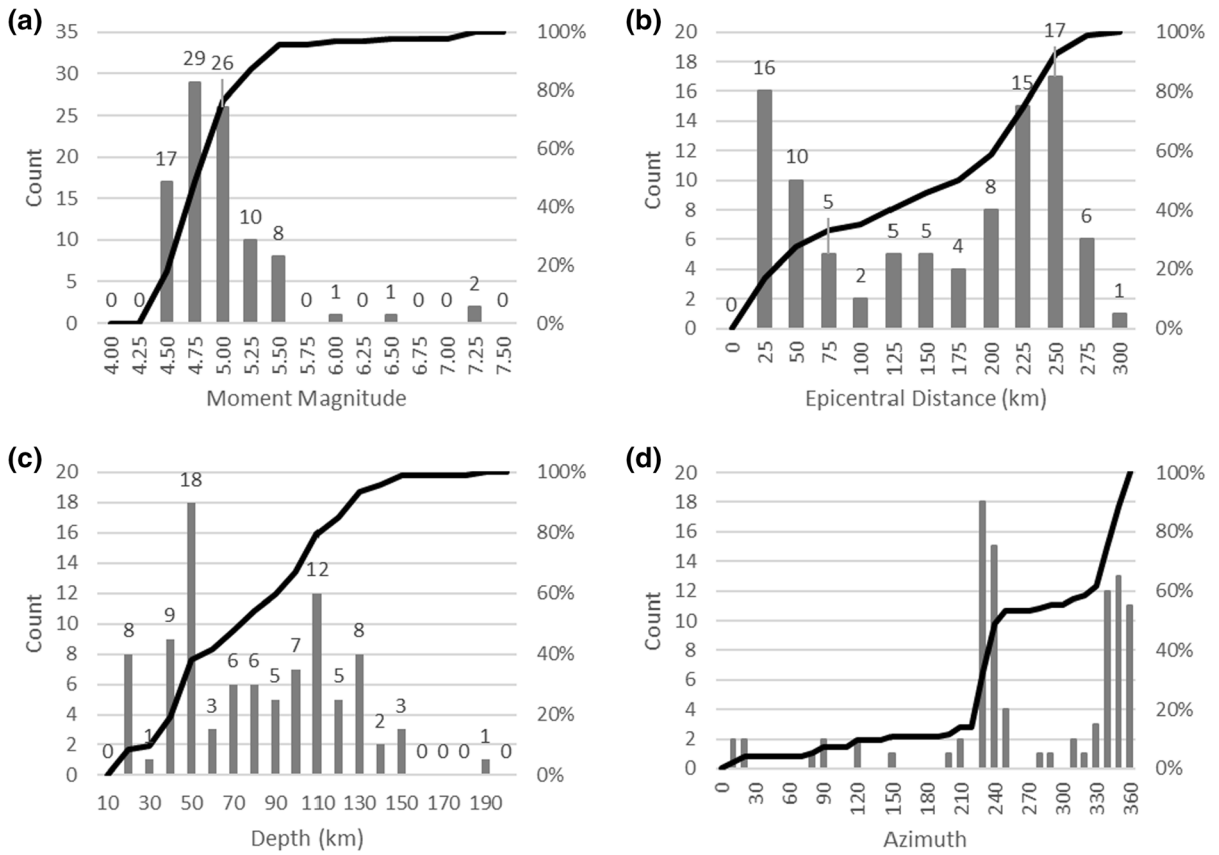


Figure 5

Summary of Database Event Parameters. **a** Magnitude distribution, **b** epicentral distance to anchorage, **c** event depth, **d** Azimuthal DIRECTION FROM ANCHORAGE. The mean value for each bin is presented on the x-axis

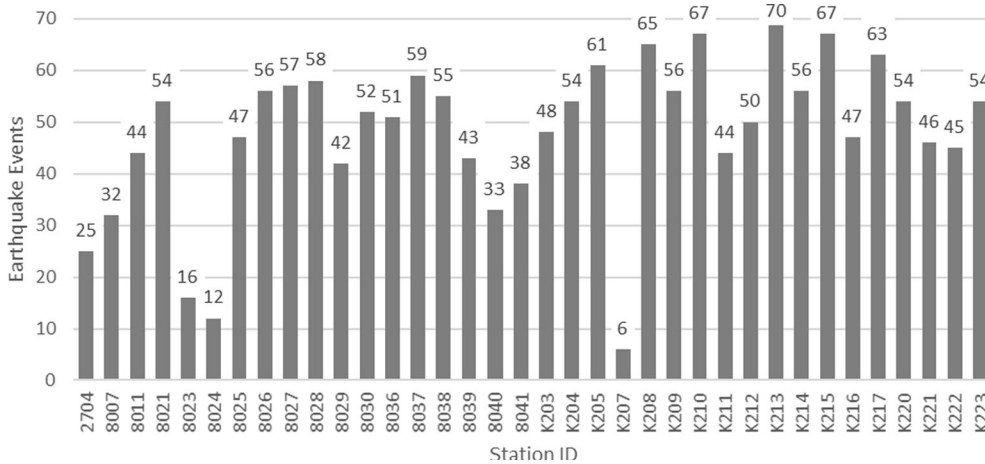


Figure 6

Number of earthquake recordings per station from 2004 to 2019 used in this study



spectrum at any site due to a source is the logarithmic summation of the source, site, and path spectra.

For this study, GITANES (Version 1.3) developed in MATLAB by Klin (2019) was used. Selected SAC format three-component time histories described in previous sections are loaded into GITANES. The program uses the data in the headers to select the S-wave portion of the time history (10 s as shown in Fig. 2) and performs a fast Fourier transform of the data. The logarithmic value of the spectral amplitude of the S-wave data can be expressed as:

$$\log A(r_{ij}, f) = \log S_{o_i}(f) + \log S_{I_j}(f) + \log P(r_{ij}, f) \quad (2)$$

where the amplitude spectrum of the recorded S-wave data,  $A$ , is a function of the hypocentral distance,  $r$ , and frequency,  $(f)$ .  $S_{o_i}(f)$  is the source for the  $i$ th source term,  $S_{I_j}(f)$  is the site term for the  $j$ th site, and  $P$  is the path effect describing the attenuation of the source hypocentral distance  $r_{ij}$  for the  $i$ th earthquake event to the  $j$ th site.

The path term ( $P$ ) can be written as:

$$P(r_{ij}, f) = \frac{1}{r_{ij}^\gamma} e^{-\frac{\pi r_{ij} f}{V_s Q_0 f^\eta}} \quad (3)$$

Taking the logarithm of the path term:

$$\log P(r_{ij}, f) = -\gamma \log(r_{ij}) - \frac{\pi r_{ij} f}{V_s Q_0 f^\eta} \quad (4)$$

where  $r_{ij}$  and  $f$  are the distance and frequency, respectively, and  $\gamma$  is the geometric spreading coefficient. The parameters  $V_s$ ,  $Q_0$ , and  $\eta$  are the average shear-wave velocity, quality factor at 1 Hz, and exponent, respectively.

One of the tradeoffs when using GITANES is that the path terms defined in Eq. 4 are constrained. For this study, the average shear wave velocity is assumed to be 3.2 km/s (Table S1 of Silwal & Tape, 2016), due to the range of shallow to deep earthquakes. The quality factor,  $Q_0$ , of 150 was used for this study and  $\eta$  was set at one. Several regional studies, including Boore (2013), McNamara (2000), and Stachnik et al. (2004) show the values of  $Q_0$  often to range between approximately 100–300 for various models of surface, coda, and shear waves. A sensitivity analysis was performed to select the  $Q_0$  and  $\eta$  values and it was found that varying them had an

insignificant effect on spectral amplification. The results of the sensitivity analysis for Station 8040 are presented in Fig. 7, as an example of a typical result. It has been observed that the choice of  $Q_0$  does not significantly affect the results of site response studies such as this one. Still, it does impact source spectra estimates (Parolai et al., 2000), which is supported by the results of the sensitivity analysis performed for this study.

The geometric spreading coefficient,  $\gamma$ , was assumed equal to 1 (spherical waves) for distances less than 100 km and 0.5 (cylindrical waves) for distances greater than 100 km, which is similar to the assumption of Dutta et al. (2003) and used for earthquakes with epicentral distances of 75–500 km in a southcentral Alaska study by McNamara (2000). The geometric spreading coefficients are also recommended by Havskov and Ottemoller (2010) when using simplified geometric spreading parameters, such as those used in GITANES. It is noted that the change in the geometric spreading coefficient should theoretically also be reflected in the time-window chosen to capture the strongest portion of ground motions (fixed at 10 s to capture the direct S-waves). As shown in the various sensitivity studies, the impact of making such a change would be negligible so it was not done for simplicity. The distance,  $r_{ij}$ , was collected from header information for each event. A sensitivity analysis, using a range for each coefficient and visual evaluation on the effects of the coefficient values on the site results, was performed before settling on these values.

Rewriting Eq. 2 as:

$$\log A(r_{ij}, f) - \log P(r_{ij}, f) = \log S_{o_i}(f) + \log S_{I_j}(f) \quad (5)$$

And substituting Eq. 4:

$$\begin{aligned} \log A(r_{ij}, f) + \gamma \log(r_{ij}) + \frac{\pi r_{ij} f}{V_s Q_0 f^\eta} \\ = \log S_{o_i}(f) + \log S_{I_j}(f) \end{aligned} \quad (6)$$

For a particular frequency we denote:

$$d_{ij} = \log A(r_{ij}, f) + \gamma \log(r_{ij}) + \frac{\pi r_{ij} f}{V_s Q_0 f^\eta} \quad (7)$$

where  $d_{ij}$  is the weighted vector with path spectrum

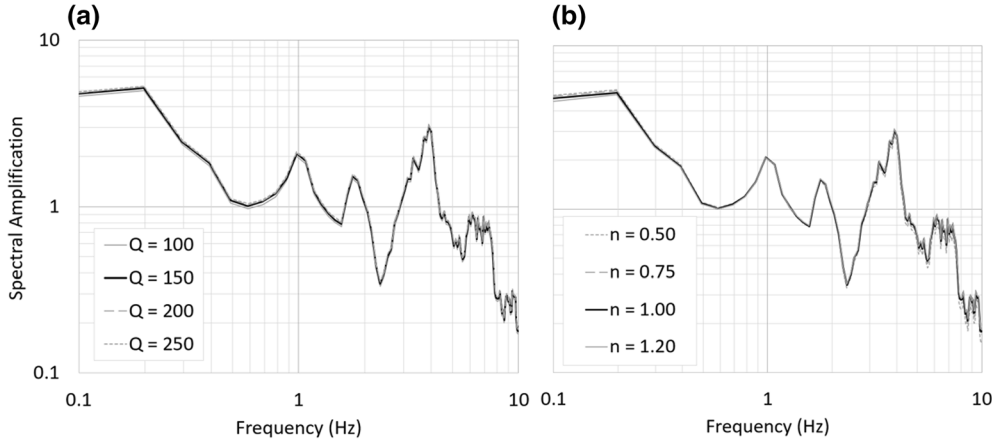


Figure 7

Sensitivity of  $Q_0$  and  $\eta$  on spectral amplification for Station 8040. **a.** Range of  $Q_0$  from 100 to 250 holding  $\eta$  at 1.00. **b.** Range of  $\eta$  from 0.5 to 1.2 holding  $Q_0$  at 150

added to the amplitude spectrum and  $\log So_i(f) = so_i$  and  $\log SI_j(f) = sj_j$ . Equation 6 can be expressed as:

$$d_{ij} = so_i + sj_j \quad (8)$$

The matrix form of Eq. 8 can be expressed as:

$$\begin{pmatrix} G \\ S \end{pmatrix} m = \begin{pmatrix} d \\ 0 \end{pmatrix} \quad (9)$$

where  $G$  is the sparse matrix that relates  $m$ , the model vector of unknown source and site terms (logarithmic values), to  $d$ , defined in Eq. 7; and  $S$  is the row matrix that is appended to matrix  $G$  with reference site terms. These matrices are solved independently for each frequency of interest.

As mentioned above the path term is constrained in GITANES but does not have an appreciable effect on the site response results. While the source spectra results are not the primary focus of this study, the source spectra have been evaluated to understand the effects of path terms  $Q_0$  and  $\eta$  and to verify their appropriateness and physical meaning. The sensitivity analysis results of  $Q_0$  and  $\eta$  on the source spectrum for the  $M_w$ 7.1 Anchorage Earthquake are presented in Fig. 8. The variability of the source spectrum with respect to  $Q_0$ , holding  $\eta$  at unity with similar results for  $Q_0$  ranging from 150 to 250 (Fig. 8a). Figure 8b shows that the variation of  $\eta$  using values between 0.5 and 1.2, while maintaining  $Q_0$  at 150, produces little impact for  $\eta$  ranging

between 0.75 and 1.2. These sensitivity results support the use of  $Q_0$  and  $\eta$  values described in the site amplification discussion above.

As shown in Fig. 9a, source spectra from the 95 earthquakes have been plotted. The source spectrum in black at the top of Fig. 9a is replotted in Fig. 9b using  $Q_0$  of 150 and three values of  $\eta$ , including 0.5, 0.75, and 1.0. Figure 9b also presents Brune's omega square model (Brune, 1970) with stress drops of 2 and 5 MPa, and a seismic moment of  $5.02 \times 10^{19}$  Nm to evaluate the source spectral shape. Estimates of stress drop range from 2.7 to 3.9 MPa and a seismic moment of  $5.02 \times 10^{19}$  Nm by Liu et al. (2019) for the  $M_w$ 7.1 Anchorage Earthquake. The results presented in Fig. 9b indicate the Brune's omega square model fits the source spectral shape for this event well, further supporting the path parameters selected for this study, given the range of earthquakes in the database. Further discussion related to calculated source spectra results has not been included in this paper for brevity.

The results of the GIT provide spectral amplification functions (SAFs) for the two horizontal components of each station from the two orthogonal components based on a selected reference station. In this study, the K216 surface station was used as the reference station. This station is located at the eastern edge of Anchorage and is in the Chugach Mountain Range on a rock outcrop. The site is underlain by

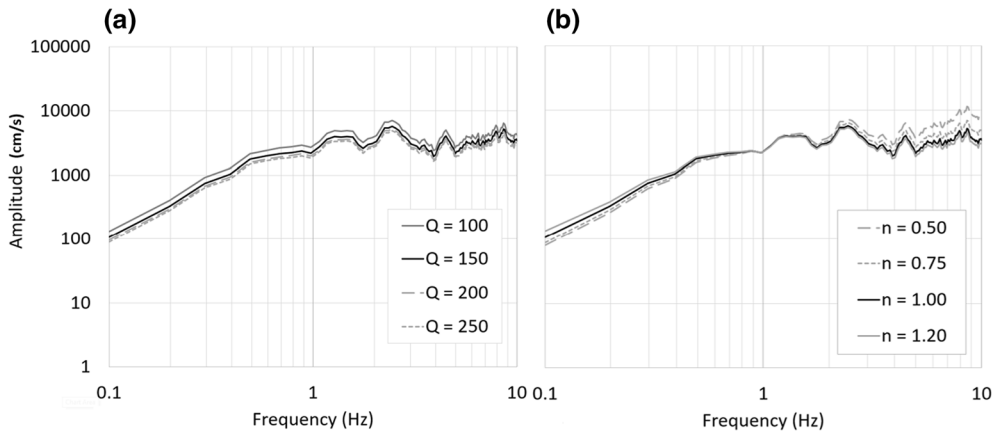


Figure 8

Sensitivity of  $Q_0$  and  $\eta$  on source spectra for the  $M_w7.1$  Anchorage Earthquake. **a.** Range of  $Q_0$  from 100 to 250 holding  $\eta$  at 1.00. **b.** Range of  $\eta$  from 0.5 to 1.2 holding  $Q_0$  at 150

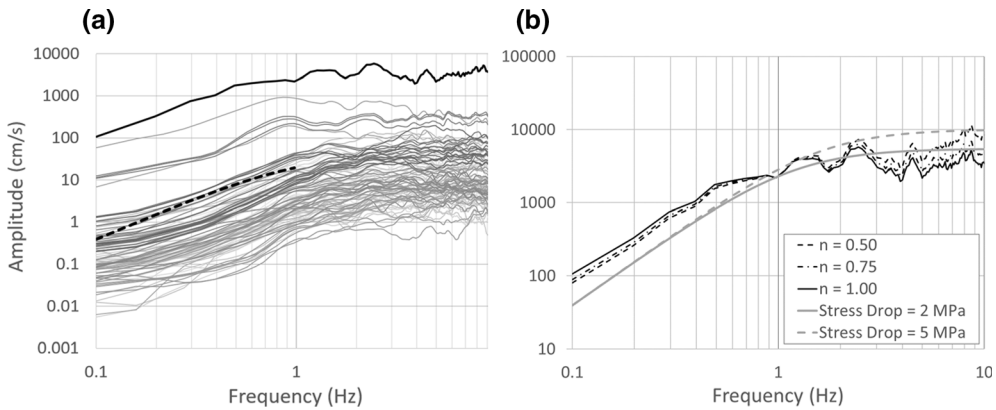


Figure 9

Source spectra calculated for this study. **a.** Source spectra for the 95 events with the  $M_w7.1$  earthquake source spectrum in black and the others in grey. The dashed black line shows the general slope of Brune's omega square model. **b.** The  $M_w7.1$  source Spectrum with  $Q_0$  of 150 and a range of  $n$  values between 0.5 and 1.0 in black. The omega square model for the event (Brune, 1970) for two stress drops in grey. Note, the y-axis scales in (a., b.) are different

glacially-carved and metamorphosed greywacke rock and is within the vicinity of the other stations. It is the best reference station available for the network as it is the stiffest site with respect to its shear-wave velocity. The other strong-motion stations are underlain by soil and were not deemed to be more effective than K216 as a reference station.

The frequencies of interest for this project range from 0.25 to 10 Hz for reasons noted earlier. When evaluating the range of frequencies, Zhu et al. (2021) suggests evaluating the site-to-site variability ( $\varphi_{S2S0}$ )

which identifies the parametric and modeling uncertainty and is independent of the reference station selection. Site-to-site variability is the standard deviation of the natural logarithm of the spectral amplifications. As shown in Fig. 10,  $\varphi_{S2S0}$  rises sharply and the variability becomes more significant after 10 Hz indicating lower uncertainty between 0.1 and 10 Hz. Additionally, the spectral amplification at several stiffer soil sites shows ratios below unity at frequencies greater than 7 Hz, suggesting that the K216 station amplifies seismic waves above 7 Hz,

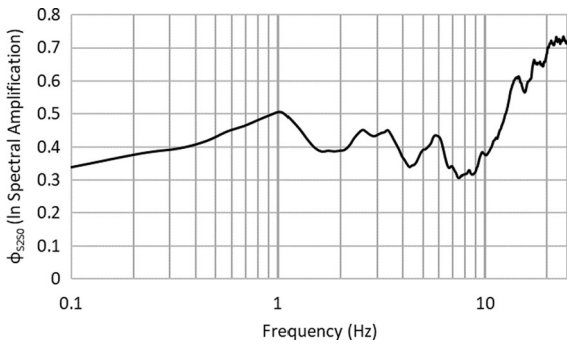


Figure 10

Site-to-site variability ( $\phi_{S2S0}$ ) for frequencies of 0.1–25 Hz for the spectral amplification results of this study

which means it may not be an ideal reference site for the entire range of frequencies used in this study. Similar findings were reported by Martirosyan et al. (2002). The horizontal-to-vertical spectral ratio (HVSr) of the strong-motion stations were calculated in GITANES and shown in Fig. 11. Further discussion of the HVSr calculations for Anchorage strong-motion stations is presented in Thornley et al. (2021b). Lower horizontal site amplifications are observed at a site when HVSr is near unity. The K216 station provides generally the lowest bound HVSr ratio among the stations (black line in Fig. 11). As an example, the blue line in Fig. 11 presents the HVSr ratio for Station 8040. There are

significant horizontal amplifications at Station 8040, showing why it would not be an effective reference station. However, at frequencies greater than 7 Hz, K216 diverges more significantly from unity and has the highest HVSr of all the stations, indicating site amplification complexities at this site above 7 Hz.

The mean spectral amplification values for the two orthogonal horizontal component SAFs and their standard errors are provided as output from GITANES. An averaging technique, as proposed by Goulet et al. (2018), was applied to the resulting orthogonal horizontal site amplification ratios to calculate a single site amplification ratio at each station that is independent of instrument orientation. The equation:

$$EAF(f) = \sqrt{\frac{1}{2} [SAF_{E-W}(f)^2 + SAF_{N-S}(f)^2]} \quad (10)$$

in which the EAF is the average site amplitude spectrum calculated at each frequency of interest ( $f$ ), and  $SAF_{E-W}$  and  $SAF_{N-S}$  are the site amplification functions for the east–west and north–south orthogonal horizontal components, respectively. This is similar to what is done for Fourier amplitude spectra (FAS) for orthogonal components within ground-motion models (Bayless & Abrahamson, 2019). From this point forward the spectral amplifications for each site have been calculated using Eq. 10.

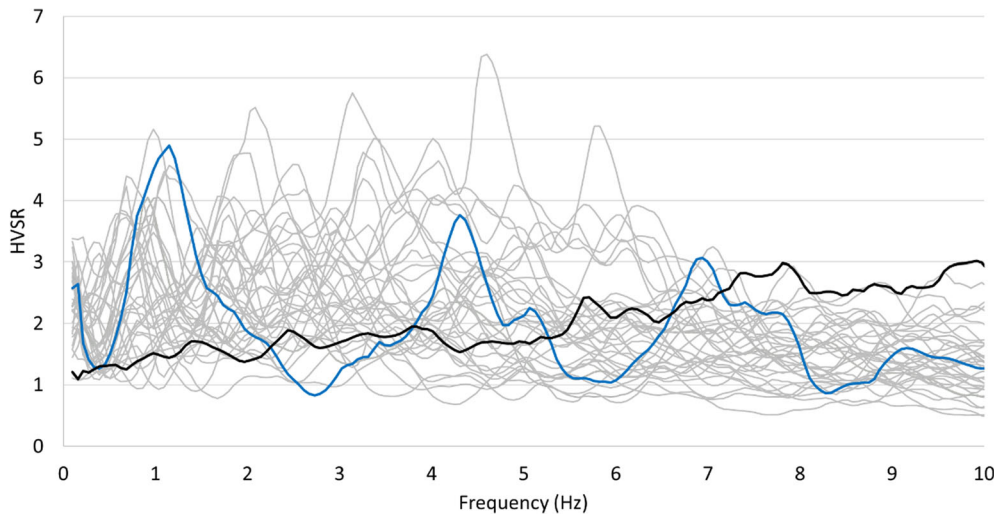


Figure 11

HVSr of the strong-motion stations used in this study. K216, the selected reference station, is the black line and Station 8040 is the blue line

#### 4.2. Sensitivity of Model

A wide variety of earthquakes are used in this study, ranging in magnitude, epicentral distance, depth, and source type. An effort has been made to better understand the impacts of these elements in the dataset on the results of the site response analysis. As an example, more than 70% of the earthquakes in the database are smaller than  $M_W$  5.0 (Fig. 5a). The dataset was subdivided into earthquakes smaller than  $M_W$  5.0 and those equal to or greater than  $M_W$  5.0. The two subdivided sets were evaluated using GIT, and the results were compared. An analysis of the residuals,  $R_{k,l}$ , was performed to evaluate the bias one dataset has compared to the other by using Eq. 11, where AmpA is the larger dataset, which in this case is the events less than  $M_W$  5.0, and AmpB is defined as the smaller dataset, with  $k$  and  $l$  being the number of the recording station and frequency, respectively. The results of the magnitude sensitivity analysis are presented in Fig. 12, with the average and the bounds of  $\pm 1$  standard deviation indicated.

$$R_{k,l} = \log(\text{AmpA}_{k,l}) - \log(\text{AmpB}_{k,l}) \quad (11)$$

The results of the magnitude analysis suggest that there is some influence of the lower magnitude data set on the results; however, zero is within one standard deviation for most of the frequencies of interest. Only for 1.8–3 Hz and 4.1–5.6 Hz is the mean more than one standard deviation above zero.

The residual analysis was also performed for epicentral distance where the division is between earthquakes less than 100 km (36%) from Anchorage versus those at distances between 100 and 300 km (64%). Sensitivity analysis considering the focal depth was also undertaken, especially given the range of earthquake depths is from 10 to 189 km. A division point was selected at a depth of 50 km, where 61% of the events were at depths greater than 50 km, and 39% are less than 50 km. It was found that, in general, there was no significant impact of epicentral distance or depth.

An additional analysis considered the impact of azimuth on the results. As shown in Figs. 4 and 5d, there are two predominant azimuthal zones in the dataset. The first is the earthquakes to the southwest of Anchorage with azimuths between  $225^\circ$  and  $250^\circ$ ,

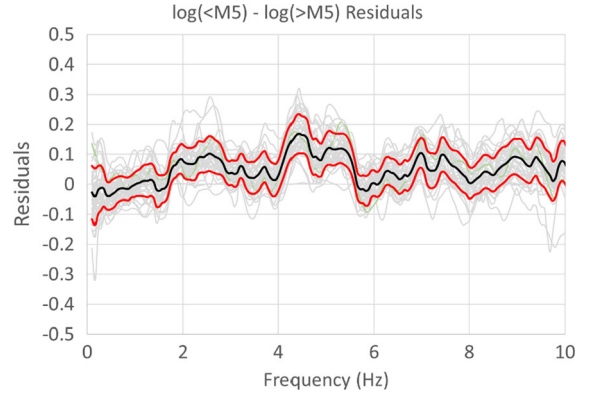


Figure 12  
Residual plot of magnitudes less than and greater than  $M_W$  5.0. The black line indicates the average and the red lines  $\pm 1$  standard deviation

and the second includes the earthquakes north-northwest of Anchorage with an azimuthal range of  $330^\circ$ – $360^\circ$ . It was found that there was minimal impact related to whether the earthquake originated in either of these locations. Figure 13 presents the results of the residual analysis for the northern azimuthal range versus the events not in that range. Similar results were observed for the southern azimuthal range. The potential biases generally correspond to less than 30% because common (base 10) logarithms are used ( $10^{0.1} = 1.26$ ). It is noted that, although this potential bias is relatively minor, more data from a variety of azimuths, magnitudes and distances would better constrain the results. While

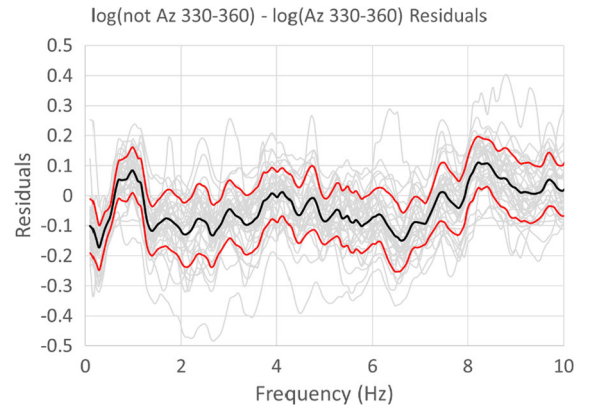


Figure 13  
Azimuthal residual results for the azimuth range between  $330^\circ$  and  $360^\circ$  degrees. The black line indicates the average, and the red lines are  $\pm 1$  standard deviation



our conclusions are not affected by this analysis, these effects should be considered for future studies if a range of azimuths cannot be achieved.

Additional sensitivity analyses were performed to evaluate the impact on the results of event type, the November 2018  $M_W$  7.1 earthquake, and other factors. These analyses suggest that the results are not sensitive to these factors. It is interesting to note that there were likely nonlinear site effects at some of the stations that recorded the November 2018  $M_W$  7.1 earthquake (Thornley et al., 2021a). To evaluate the effects of this event on the overall results of the study, the GIT was repeated on the full database and the full database without the data from the  $M_W$  7.1 event. The two sets of results were compared for each strong-motion station where the  $M_W$  7.1 event was recorded and it was found that there was very little change (less than 4%) in the overall results, which is attributed to the large number of events in the database. Figure 14 presents the results for three stations, one in each of Site Classes C, CD, and D. The site classes are defined by time-averaged shear wave velocities in the upper 30 m ( $V_{S30}$ ), where Site Class C is 440–640 m/s, Site Class CD is 300–440 m/s, and Site Class D is 215–300 m/s (BSSC, 2019). Site Class D sites showed nonlinear response from the  $M_W$  7.1 event; however, none of the stations show any significant difference between the database with and without the  $M_W$  7.1 event (less than four percent difference at any frequency).

### 5. Site Response

As described above, there is significant geologic variability across Anchorage, which as shown by others including Souriau et al. (2007) can impact site effects across a region. That geologic variability results in nonuniform site response, where different areas of the city behave differently during strong shaking. There is a need to understand and model this variability so that better risk-mitigation decisions can be made by policymakers, engineers, and emergency response teams. The results from the GIT provide insights into those differences. For example, as shown in Fig. 15, there are significant differences in site response, as indicated by spectral amplification,

between a site (K209) located in east Anchorage where the near-surface soils are dense glacial till overlying rock versus the DPDA site (8040), located in the center-north portion of the city, where there are more than 45 m of alluvium and BCF silts and clays overlying glacial till (Thornley et al., 2019). The spectral amplitude results for each station are included in “Appendix C”. Twelve of the 35 stations presented in this study were evaluated by Dutta et al. (2003) using the GIT methodology, but with a different database of earthquakes, as described earlier. The results of that study for those stations are compared with the spectral amplification results from this study in “Appendix C”. In general, there is a good fit between the results from Dutta et al. (2003) and this study, where the average spectral amplification results of the past study stay within the standard error of the results of this study. There are three stations, K203, K220, and K221 where there is a difference at one frequency, but the results across the other frequencies at these stations also fit well within the standard error of the results from this study.

While acknowledging the geologic variability across Anchorage, it is important to identify areas of similarity among specific frequencies of interest. The focus of this study was to evaluate the spectral amplitudes for a range of frequencies between 0.25 and 10 Hz, with the understanding that frequencies above 7 Hz may be artificially low because of potential site amplifications at K216. To more clearly show similarities and differences across Anchorage the 1 Hz and 5 Hz frequencies were considered for further evaluation. These two frequencies of interest were selected because of their use in engineering studies; these frequencies are often used in engineering studies to define design response spectra (American Society of Civil Engineers, 2017). As shown in Fig. 16, there is a chance that the value at exactly 1 Hz may not be representative of the values above and below 1 Hz. A logarithmic-band average of the computed spectral amplifications was, therefore, used between 0.5 and 2.5 Hz for the 1 Hz band and logarithmic-band average between 4 and 6.5 Hz for the 5 Hz band, which is also shown in Fig. 16.



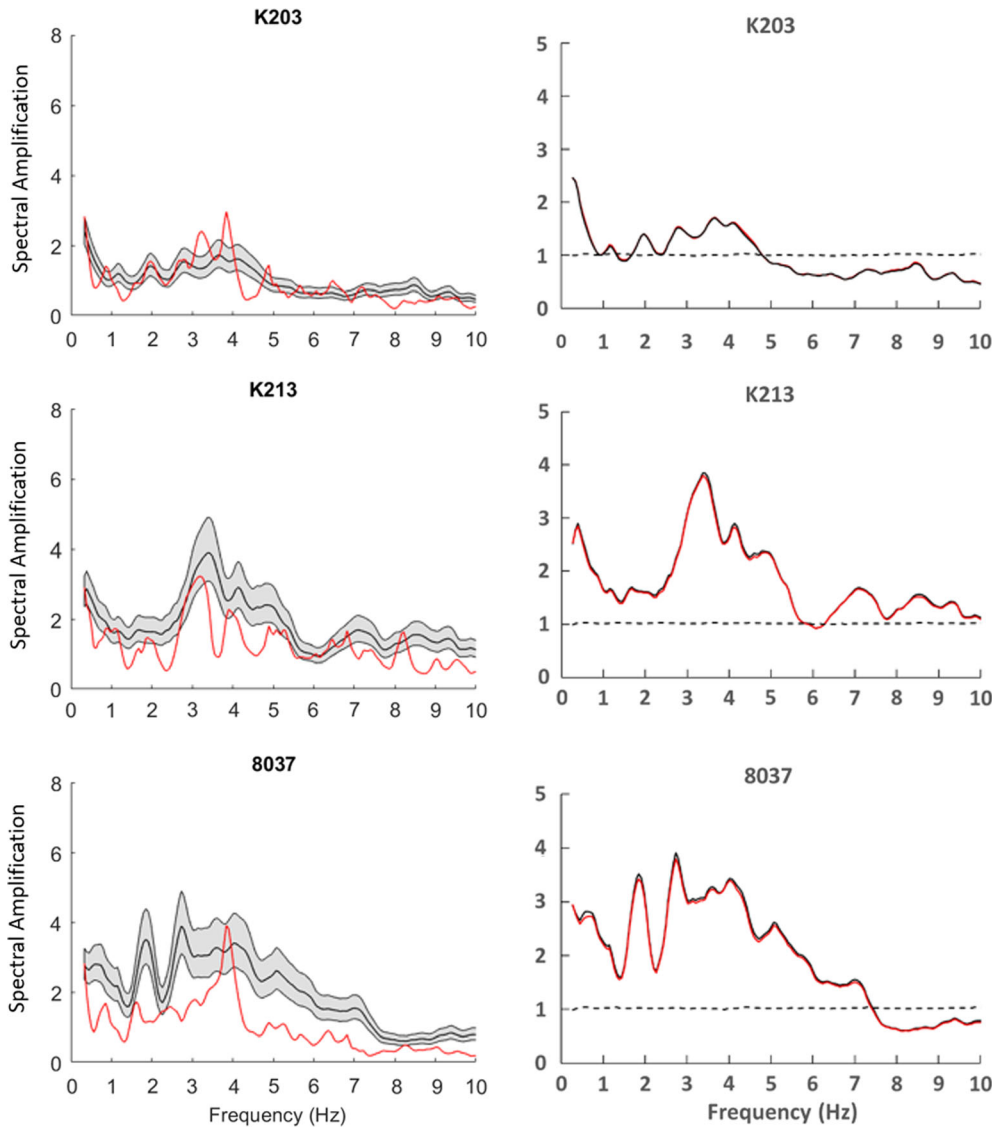


Figure 14

Spectral amplification results for Stations K203 (Site Class C), K213 (Site Class CD), and 8037 (Site Class D). On the left-hand side, the spectral amplifications for all events excluding the  $M_w$  7.1 event are in black with the grey shading presenting the standard error and the red line presenting the spectral amplification from the  $M_w$  7.1 event. On the right-hand side the spectral amplifications of the database with and without the  $M_w$  7.1 event included (red line with and black line without), and the dashed line the ratio of the two (i.e., database without/database with)

### 5.1. Spectral Amplification Variability Across Anchorage

The strong-motion stations are roughly uniformly distributed across Anchorage, from shallow soil over the rock in the eastern portion of the city to the deep soil deposits in the mid to western portions of the city. To highlight the changes in spectral

amplification across the city for the specific frequency ranges, two contour maps are drawn. The contours were created using GIS software by applying an inverse distance weighting with a power of three. No smoothing was applied. The contours have not been modified to account for known changes in surficial geology between stations. Due to the high

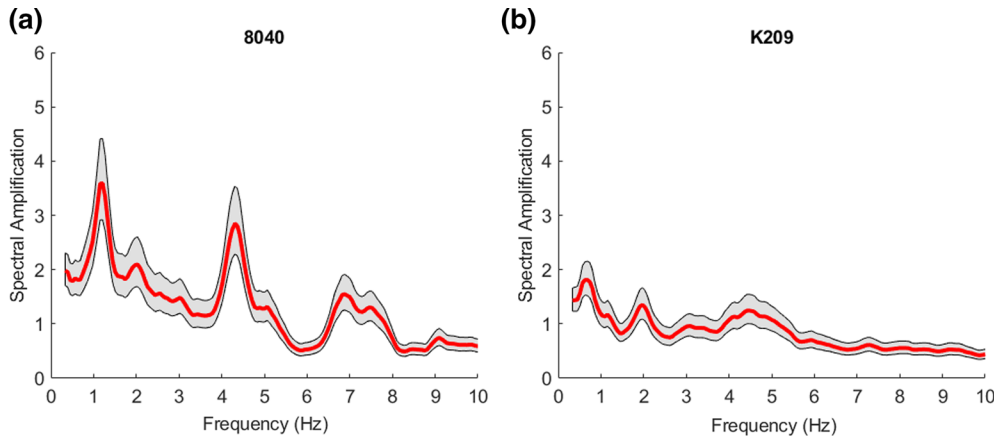


Figure 15

Spectral amplifications of two sites **a** DPDA station (8040) in north-central Anchorage and **b** Station K209 in east Anchorage. The average spectral amplification is indicated by the red line and the standard error is indicated by the shaded area above and below the average. Amplifications are relative to the reference station

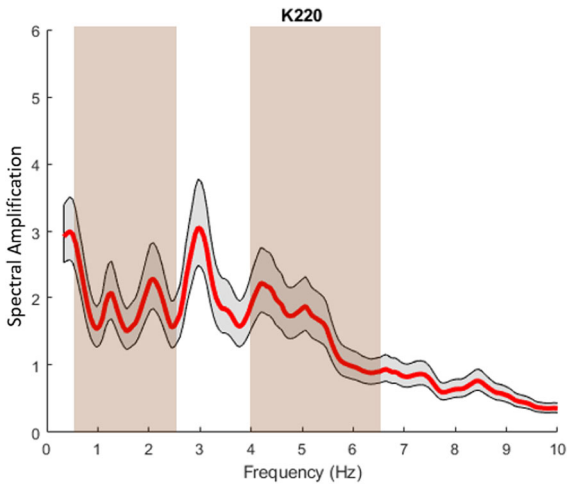


Figure 16

Spectral amplification at the K220 Station—the western-most station used in this study. The vertical left shaded band is the range of the 1 Hz band average and the vertical right shaded band is the range of the 5 Hz band average

density of the strong-motion stations across Anchorage the variability of subsurface geology is generally accounted for by these contours. Trends in the contours can be seen, and initial conclusions are drawn below; however, it is acknowledged that location-specific responses may be different due to variability of surficial geology. Contour maps for 1 Hz and 5 Hz are presented in Figs. 17 and 18.

There is a general trend across Anchorage for the 1 Hz band-averaged spectral amplification. The spectral amplification of the stations compared to the reference station is less than 1.5 in the eastern portion of the city and increases to the west. Combellick (1999) presents a line that estimates the eastern extent where the BCF (primarily silt and clay) becomes less than 10 m thick. That estimated line is shown in Figs. 17 and 18. The thickness increases to the west and then decreases in thickness again at the western edge of the city as indicated by Ulery and Updike (1986). In general, the spectral amplification at 1 Hz appears to increase as the BCF increases with depth and then decreases again at the western edge of the city.

Boreholes near Stations K221 and K208 indicate cohesive soil depths of 25 and 20 m, respectively. The amplifications observed at 1 Hz for Stations K208 and K221 are similar in both this study and that of Dutta et al. (2003). Similarities like this show that, despite two different datasets, the estimated low-frequency amplification tends to be similar. However, Station 8039, a newer station not included in Dutta et al. (2003), in southwest Anchorage, has the highest spectral amplification (3.9) at 1 Hz. Ulery and Updike (1983) indicate the BCF has deeper regions of cohesive soil in the vicinity of this site. Station 8039 is located in an area that has approximately 55 m of cohesive BCF soil below it. Interestingly,

## Site Response Analysis of Anchorage

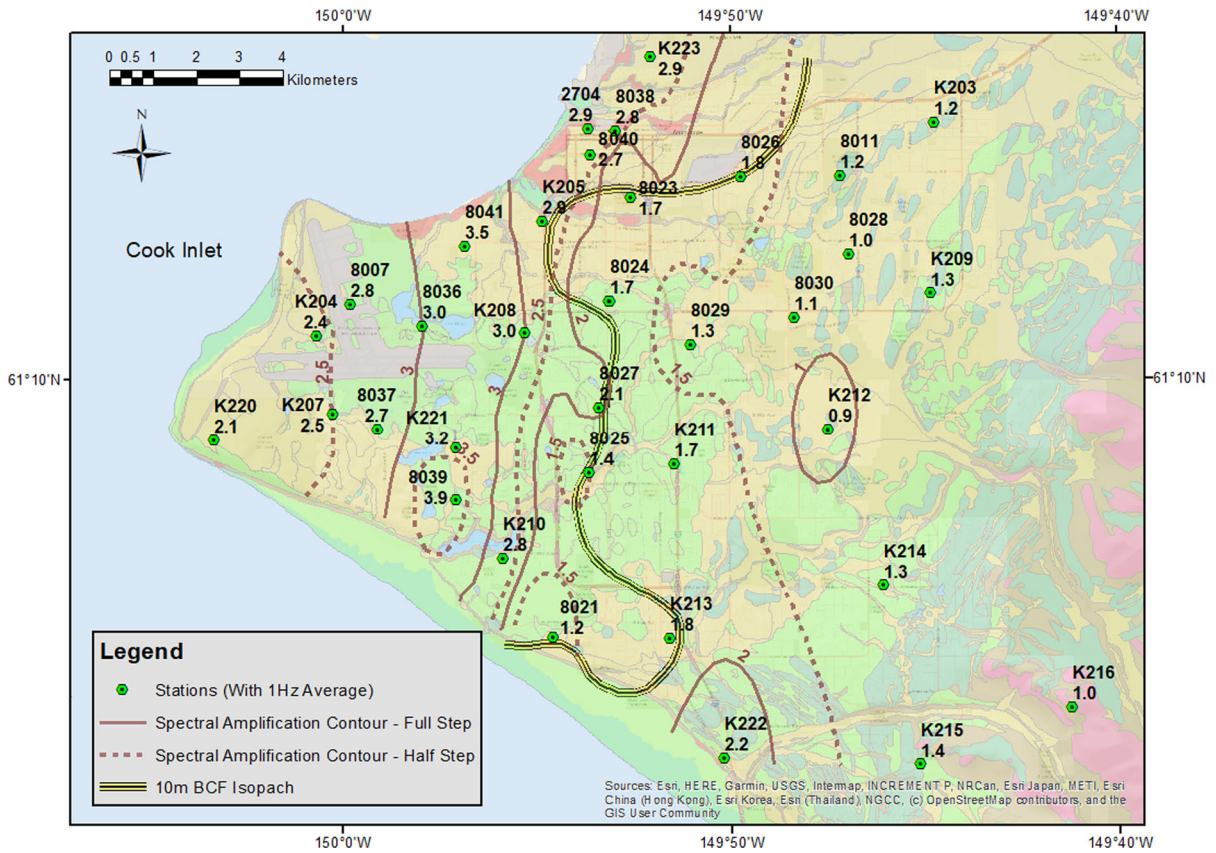


Figure 17

1 Hz band-averaged spectral amplification contour map. Contours are in 0.5 spectral amplification units. The stations are indicated along with their band average spectral amplification for 1 Hz frequency

Station 8041 is located in another area with a deeper cohesive soil deposit of 45 m and a band-average spectral amplification of 3.5 at 1 Hz. The results at the western edge of the city tend to show lower amplifications (e.g., K220 in this study has a spectral amplification of 2.1 while Dutta et al. (2003) shows a spectral amplification of 2.7), which is also where the soft portions of the BCF become thinner and stiffer soil becomes more predominant (Updike & Ulery, 1986). Based on the findings from this study, the thickness of the BCF directly impacts the spectral amplification at 1 Hz, indicating that for sites located in central to western Anchorage there is a spectral amplification of more than a factor of two.

For the higher frequency band surrounding 5 Hz, there is less of an east–west contrast (Fig. 18). On the east side of Anchorage, the spectral amplification is

similar to the reference site. There are two areas where the spectral amplification is above 2. The northern area is located in the Chester Creek basin (identified in Fig. 1) where the stations are located in an area with a mixture of alluvium and glacio-fluvial surficial soil. The second area is found in southwestern Anchorage where the surficial soils tend to consist of lacustrine or eolian silt, fine sand, and clay related to glacio-estuarine deposition (Combellick, 1999). The additional strong-motion stations that have been included in this study offer a significant improvement in the 5 Hz results compared to Dutta et al. (2003). This is particularly true in southwestern Anchorage where there are more significant amplifications (greater than 4) than were estimated by the previous study (approximately 2). The differences presented in this study are primarily related to the additional

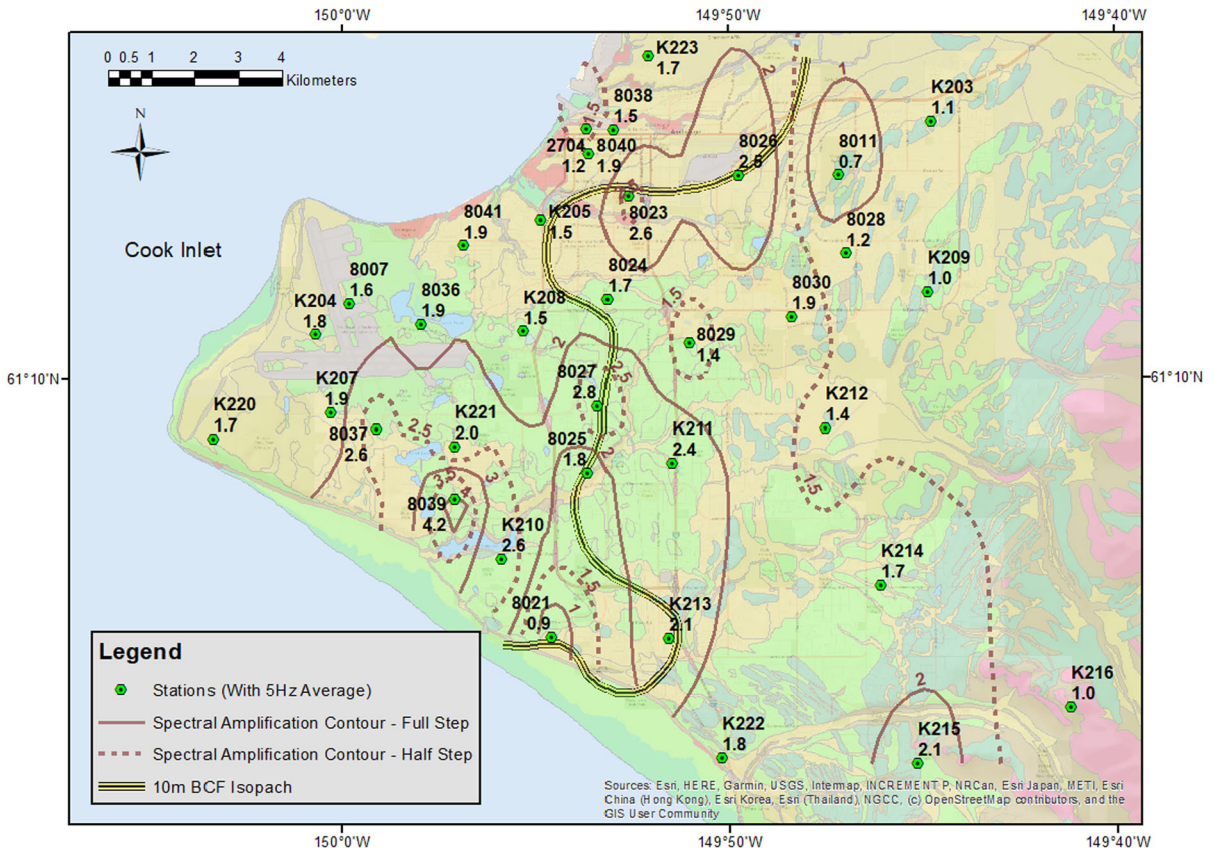


Figure 18

5 Hz band-averaged spectral amplification contour map. Contours are in 0.5 spectral amplification units. The stations are indicated along with their band average spectral amplification for 5 Hz frequency

strong-motion stations installed in key geologic conditions, further underscoring the importance of establishing and maintaining dense networks in urban areas with complex geologic conditions.

5.2. Geological impacts on Spectral Amplification

To further evaluate the impact of geology, the spectral amplifications are plotted and compared with geologic cross-sections developed by Combellick (1999). Figures 19 and 20 present the spectral amplification for several stations along a north–south and east–west geologic section, respectively. The locations of the cross-sections are indicated as dashed lines in Fig. 1. The glacial till is represented in blue, BCF soil in green and pink indicates the estimated bedrock. Other colors represent the mixture of

alluvial and other surficial soil deposits. The spectral amplification plots are centered at the locations of the strong-motion stations located along the cross-section. In areas where glacial till is shallow there is a distinct difference in the shape of the spectral amplification, especially when compared to areas where the glacial till is deep.

A third cross-section is presented in Fig. 21. This represents the NW/SE cross-section by Combellick (1999), with its location identified in Fig. 1. It offers an excellent example of the impact of soil thickness and change in response based on the type of soil. The spectral amplification starts increasing significantly in the northwest portion of the cross-section at stations located over the BCF (green) subsurface soil. This contrasts with the stations in the southeast, where the



## Site Response Analysis of Anchorage

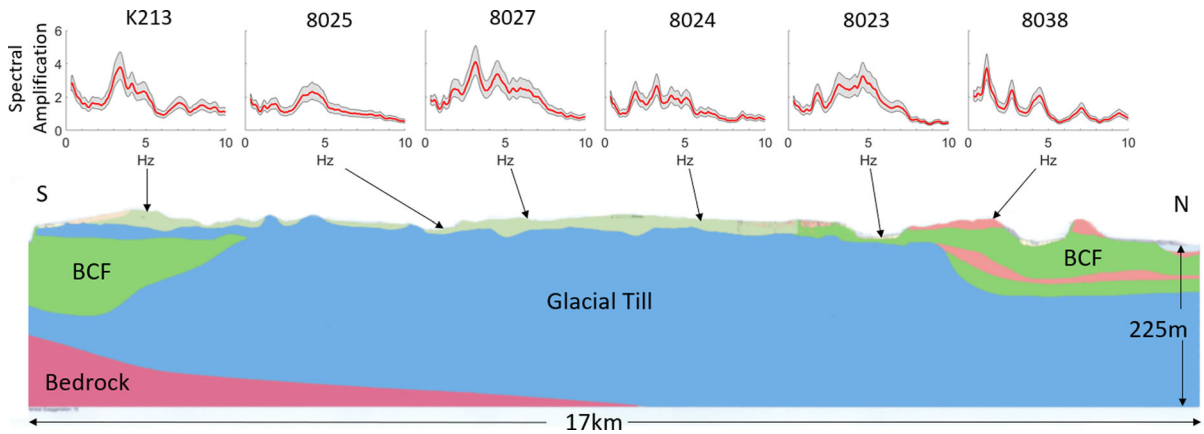


Figure 19

North-South Geologic Cross Section (South is on the left side of the figure). Geologic Cross Section from Combellick (1999) C Street section. Vertical and horizontal spectral amplification plot axes are the same on all plots

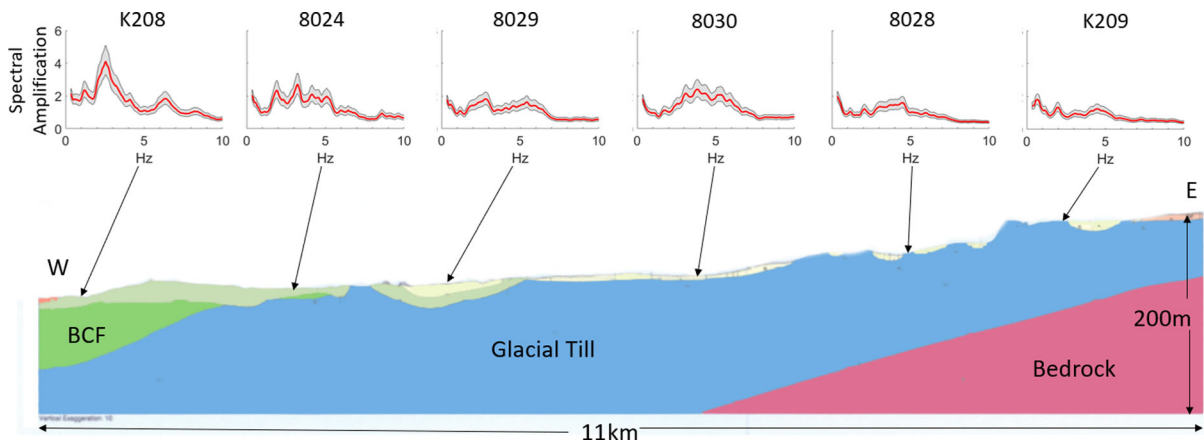


Figure 20

East-West Geologic Cross Section (West is on the left side of the figure). Geologic Cross Section from Combellick (1999) Tudor section

stations are located with dense to very dense glacial till close to the surface.

### 6. Conclusions

The results of this study build on past studies and provide further insight into the variability of site response through an evaluation of the spectral amplification of ground motions at strong-motion stations in Anchorage. The dataset used in this study is independent of previous studies and includes various events from magnitudes  $M_W$  4.5–7.1. There is a

strong geological effect on the response of different areas in Anchorage. As seen in Figs. 17 and 18, there will be distinct impacts on structures with varying frequencies of response in future earthquakes. The results provide additional insight into which areas in Anchorage are susceptible to higher ground motions, due to the subsurface (and potentially other factors, such as topography) conditions present.

The findings of this study further indicate that the BCF substantially impacts site response, especially at frequencies around 1 Hz. The results fit well with the geologic observations related to the extent and variable thickness of that deposit. Furthermore, the

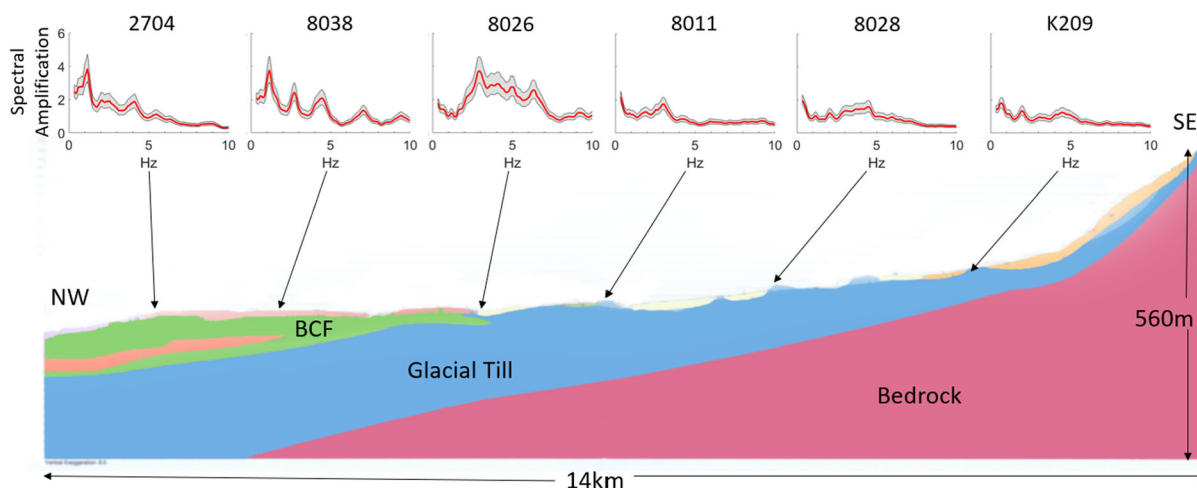


Figure 21

Northwest-Southeast Geologic Cross Section (northwest is on the left side of the figure). Geologic Cross Section from Combellick (1999) NW/SE section

results from the 5 Hz study also match well with the surficial geology, where in the southern portion of the city, the BCF is overlain by silt and sand and was in a different depositional environment compared to the northern and eastern portions of the city.

As presented in the discussion of the model sensitivity, the inclusion of a wide variety of data appears not to bias the study results. While it is acknowledged that the dataset would be better if larger and closer earthquakes were included, no such data exists at this time. The sensitivity study indicates that, for several different parameters, impacts on the results were not observed. This gives confidence that the results can be used to evaluate the potential response related to larger and more damaging events.

In general, the current study agrees well with previous studies, including Dutta et al. (2003). This and the previous work are based on very different earthquake datasets and use different software, so in that way, this study validated the work performed by the previous study. This study does provide additional refinement and identifies areas where higher amplifications have been recently measured through the inclusion of additional strong-motion stations. Further investigation will be required to evaluate the impact of the site amplifications on the built environment—this study provides support to perform those analyses.

### Acknowledgements

The authors would like to extend their appreciation to several individuals. The dataset provided by AEC would not have been possible without the help of Natalia Ruppert, Mike West, and Mitch Robinson. The DPDA data is supported by the tireless efforts of Jamie Steidl and the team at the University of California Santa Barbara. Andy Garrigus of Golder Associates Inc. provided support and guidance in the development of several of the figures. In addition, Peter Klin of the Italian National Institute of Oceanography and Applied Geophysics, Center for Seismological Research, provided helpful guidance in using the GITANES MATLAB program. Finally, we thank Chuanbin Zhu and an anonymous reviewer for detailed and constructive comments on an earlier version of this study.

**Author Contributions** All authors contributed to the study conception and design. Material preparation, data collection and analysis were performed by JT, supported by JD and UD. The first draft of the manuscript was written by JT and all authors commented on previous versions of the manuscript. All authors read and approved the final manuscript.



*Funding*

Not applicable.

*Availability of data and material*

Referenced in manuscript.

*Code availability*

Referenced in manuscript.

**Declarations**

**Conflicts of interest** Not applicable.

**Open Access** This article is licensed under a Creative Commons Attribution 4.0 International License, which permits use, sharing, adaptation, distribution and reproduction in any medium or format, as long as you give appropriate credit to the original author(s) and the source, provide a link to the Creative Commons licence, and indicate if changes were made. The images or other third party material in this article are included in the article’s Creative Commons licence, unless indicated otherwise in a credit line to the material. If material is not included in the article’s Creative Commons licence and your intended use is not permitted by statutory regulation or exceeds the permitted use, you will need to obtain permission directly from the copyright holder. To view a copy of this licence, visit <http://creativecommons.org/licenses/by/4.0/>.

*Appendix A*

List of stations

Station code	Latitude (°N)	Longitude (°W)
K203	61.22007	149.7453
K204	61.17581	150.0114
K205	61.19963	149.9138
K207	61.15957	150.0044
K208	61.17646	149.9215
K209	61.18455	149.7471
K210	61.12923	149.931
K211	61.14905	149.8578
K212	61.15622	149.7916
K213	61.11262	149.8595
K214	61.12353	149.7677
K215	61.08625	149.7521
K216	61.09806	149.6867
K217	61.39589	149.5154
K220	61.15404	150.0553
K221	61.15245	149.951

**Appendix** *continued*

Station code	Latitude (°N)	Longitude (°W)
K222	61.08757	149.8366
K223	61.2338	149.8675
2704	61.21883	149.894
8007	61.18236	149.9968
8011	61.20898	149.7857
8021	61.11293	149.9095
8023	61.20469	149.8762
8024	61.18314	149.8853
8025	61.14716	149.8939
8026	61.2089	149.8289
8027	61.16087	149.8894
8028	61.19264	149.7823
8029	61.17392	149.8503
8030	61.17949	149.8058
8036	61.17794	149.9657
8037	61.15625	149.985
8038	61.21844	149.8829
8039	61.14162	149.9512
8040	61.2135	149.893
8041	61.19438	149.9471

*Appendix B*

List of events

Date	Latitude (°N)	Longitude (°W)	Depth (km)	Magnitude (M <sub>w</sub> )
2/16/2005	61.3258	149.8529	34.8	4.6
4/6/2005	61.4540	146.5177	16.67	4.8
4/17/2005	60.7708	149.3106	27.49	4.5
5/19/2005	60.0168	152.6930	95.52	5.4
8/15/2005	60.1296	152.6751	102.52	4.5
3/3/2006	59.7910	153.0617	99.17	4.8
3/17/2006	60.7058	152.0240	81.07	4.7
6/18/2006	61.9256	150.4273	60.84	4.7
7/27/2006	61.1554	149.6776	35.99	4.7
9/6/2006	61.6213	149.9302	40.69	4.5
9/19/2007	61.3753	146.1054	30.82	4.5
11/28/2007	61.9108	151.1273	69.61	5.0
3/27/2008	59.0095	152.1691	68.53	5.3

Appendix *continued*Appendix *continued*

Date	Latitude (°N)	Longitude (°W)	Depth (km)	Magnitude (M <sub>W</sub> )
4/26/ 2008	63.0201	151.5561	12.45	4.6
9/18/ 2008	59.5029	152.7928	90.15	4.5
10/8/ 2008	60.1154	152.6403	103.63	4.8
10/12/ 2008	63.1608	150.5532	122.76	4.6
11/9/ 2008	59.9967	153.0191	127.14	5.0
11/29/ 2008	63.1105	149.5765	94.67	4.7
12/13/ 2008	60.8864	150.8590	46.17	4.6
12/28/ 2008	62.3457	151.0546	89.31	4.7
1/24/ 2009	59.4302	152.8875	97.87	5.8
2/15/ 2009	61.6029	146.3337	37.24	4.5
4/7/2009	61.4542	149.7428	33.03	4.8
4/10/ 2009	63.4948	151.7374	14.37	4.7
4/14/ 2009	60.1578	153.0567	117.78	4.5
4/30/ 2009	58.9929	151.3109	52.73	5.0
5/24/ 2009	59.7754	153.2489	125.48	4.6
6/22/ 2009	61.9391	150.7040	64.59	5.4
8/19/ 2009	61.2279	150.8579	66.44	5.1
4/7/2010	61.5795	149.6519	35.32	4.6
5/24/ 2010	59.9819	152.3107	71.47	4.6
7/8/2010	61.8052	150.5047	14.86	4.8
8/14/ 2010	59.9649	153.2094	141.02	4.6
9/15/ 2010	59.8613	153.1756	120.99	5.0
9/20/ 2010	61.1147	150.2192	45.43	4.9
1/23/ 2011	63.5420	150.8652	15.7	5.2
2/4/2011	60.7248	150.2764	40.85	4.5
7/28/ 2011	62.0485	151.3030	86.53	5.3
1/13/ 2013	60.5409	152.9043	133.81	5.0
3/13/ 2013	62.5560	151.2302	84.4	4.7
8/1/2013	60.1450	152.9180	126.4	4.8
8/27/ 2013	63.2129	150.6235	127.9	4.9

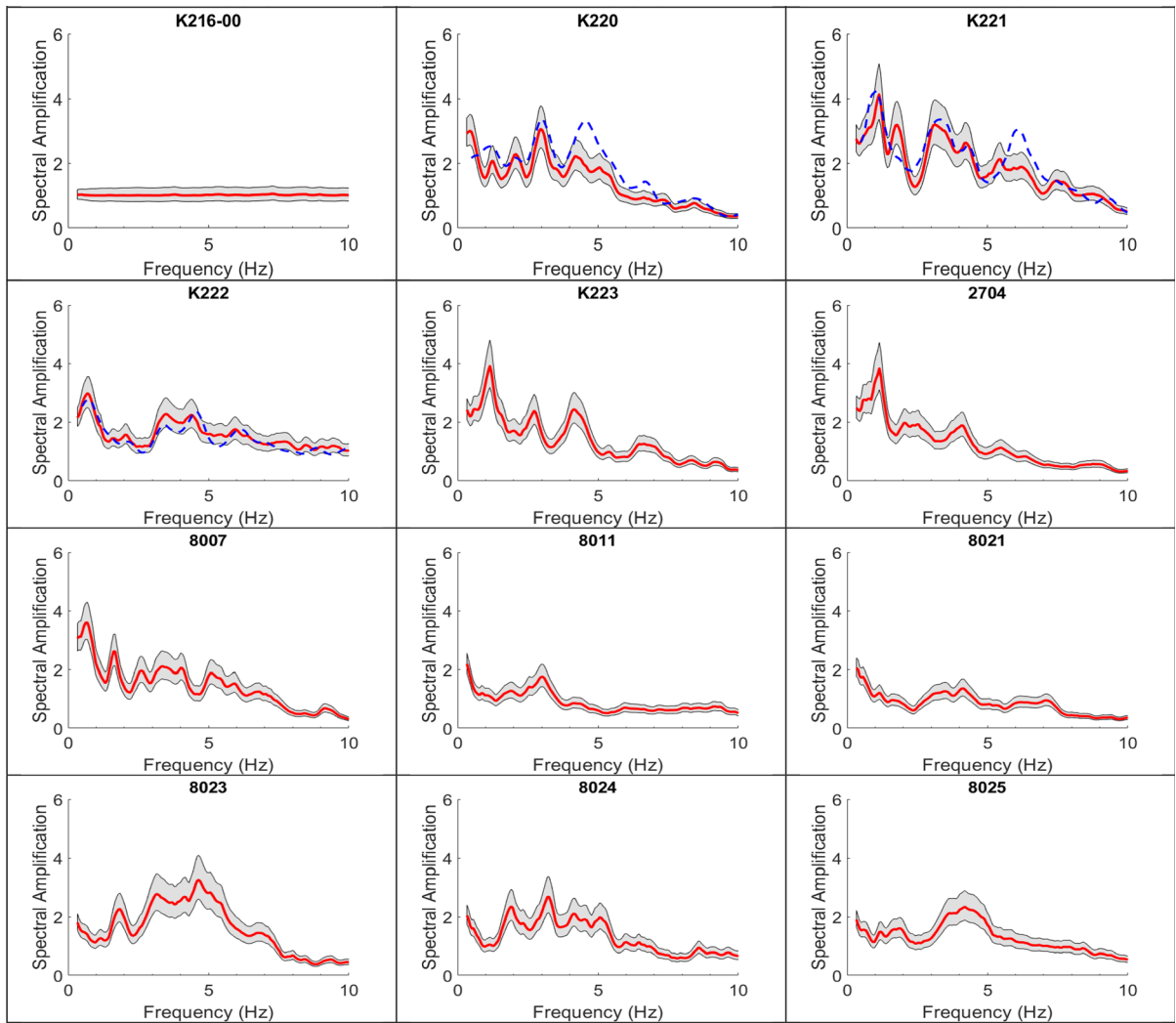
Date	Latitude (°N)	Longitude (°W)	Depth (km)	Magnitude (M <sub>W</sub> )
3/12/ 2014	59.2956	153.1770	86.1	4.5
3/30/ 2014	62.2240	151.1440	72	5.1
7/6/2015	62.1300	150.7890	70.7	4.9
7/25/ 2015	61.9493	152.0517	125.6	5.1
7/29/ 2015	59.8935	153.1961	119.3	6.3
1/18/ 2016	62.1032	150.6399	10.1	4.5
1/24/ 2016	59.7192	153.1677	107.1	4.6
1/24/ 2016	59.7312	153.1456	106.8	4.9
1/24/ 2016	59.6204	153.3392	125.6	7.1
1/25/ 2016	59.7436	153.1579	108.19	4.5
1/28/ 2016	59.6994	153.1661	107.3	4.6
2/3/2016	60.3334	153.5460	188.8	4.6
2/9/2016	59.7880	152.9746	108.3	4.5
2/10/ 2016	59.7193	153.1663	105.5	4.5
2/10/ 2016	59.7134	153.1543	105.6	4.6
3/12/ 2016	60.2609	152.3040	99.8	4.7
1/26/ 2017	62.0083	152.3898	141.9	4.5
1/31/ 2017	63.0705	150.9059	116.5	5.4
3/2/2017	59.5785	152.6546	78	5.3
4/29/ 2017	63.1225	151.1656	11.9	5.0
5/7/2017	60.1828	151.6803	66.6	5.0
5/30/ 2017	60.8382	151.8277	78.4	5.1
8/11/ 2017	60.0665	152.4770	95.5	4.8
8/31/ 2017	63.0124	150.5375	104.8	4.5
10/19/ 2017	59.7445	153.1315	101.7	4.8
11/5/ 2017	60.2253	153.0759	139.6	4.9
11/27/ 2017	60.5552	147.4303	16.6	5.1
3/9/2018	59.7509	153.1258	100.2	4.9
7/1/2018	63.0676	150.7973	117.3	4.9
7/10/ 2018	62.9789	150.6358	113.4	4.9
10/15/ 2018	61.2868	150.5223	72.1	4.5

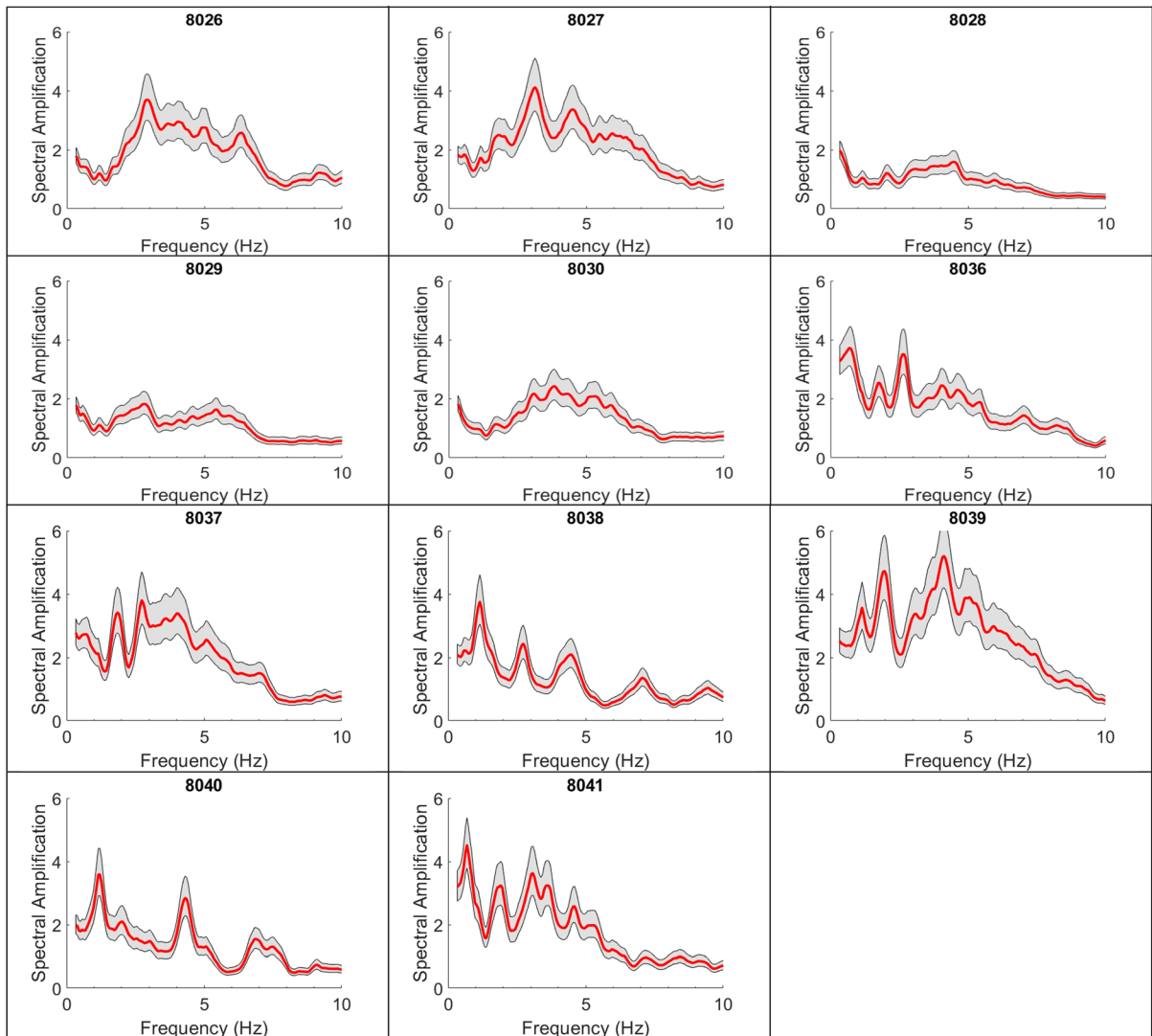
Appendix *continued*

## Appendix C

Date	Latitude (°N)	Longitude (°W)	Depth (km)	Magnitude (M <sub>w</sub> )
11/21/ 2018	59.9550	153.2658	143.3	5.5
11/30/ 2018	61.3978	149.9980	47	4.5
11/30/ 2018	61.4786	149.9231	37.2	4.5
11/30/ 2018	61.2833	149.9082	45.8	4.8
11/30/ 2018	61.3840	150.0795	37.7	4.9
11/30/ 2018	61.4590	149.9541	40.2	5.2
11/30/ 2018	61.2822	149.9571	40.8	5.5
11/30/ 2018	61.3464	149.9552	46.7	7.1
12/1/ 2018	61.4731	149.8976	34.4	4.5
12/1/ 2018	61.3760	149.9781	44.8	4.5
12/1/ 2018	61.4833	149.9362	51.3	4.9
12/1/ 2018	61.3548	149.9913	42.9	5.0
12/2/ 2018	61.3253	149.9008	51.7	4.5
12/4/ 2018	61.3941	150.0763	38.3	4.5
12/5/ 2018	61.3227	150.0534	41.8	4.5
12/6/ 2018	61.3407	149.9550	43.2	4.7
12/9/ 2018	61.4201	149.8368	41.2	4.7
1/1/2019	61.2975	149.9523	44.4	4.9
1/11/ 2019	61.4708	149.8991	49.8	4.5
1/13/ 2019	61.2993	150.0647	44.8	4.9
1/23/ 2019	61.5030	150.2373	45.5	4.5

Spectral Amplification Plots for the 35 Stations in this study. Twelve of the Stations in this study were also included in Dutta et al. (2003). The spectral amplification results from that study are included on the relevant Stations with a dashed blue line. The spectral amplification results used in these plots are also published as a data set by Thornley et al. (2021c)





**Publisher's Note** Springer Nature remains neutral with regard to jurisdictional claims in published maps and institutional affiliations.

#### REFERENCES

- Akkar, S., & Bommer, J. J. (2006). Influence of long-period filter cut-off on elastic spectral displacements. *Earthquake Engineering Structural Dynamics*, 35, 1145–1165. <https://doi.org/10.1002/eqe.577>
- American Society of Civil Engineers (ASCE). (2017). *ASCE/SEI 7-16 minimum design loads and associated criteria for buildings and other structures*. American Society of Civil Engineers.
- Andrews, D. J. (1986). Objective determination of source parameters and similarity of earthquakes of different size, in Earthquake source mechanics. In S. Das, J. Boatwright, & C. H. Scholz (Eds.), *American geophysical monograph 37* (Vol. 6, pp. 259–267). Wiley.
- Bayless, J., & Abrahamson, N. A. (2019). An empirical model for the interfrequency correlation of epsilon for fourier amplitude spectra. *Bulletin of the Seismological Society of America*, 109(3), 1058–1070. <https://doi.org/10.1785/0120180238>
- Bindi, D., Spallarossa, D., & Pacor, F. (2017). Between-event and between-station variability observed in the Fourier and response spectra domains: Comparison with seismological models. *Geophysical Journal International*, 210, 1092–1104. <https://doi.org/10.1093/gji/ggx217>
- Biswas, N., Martirosyan, A., Dutta, U., Papageorgiou, A., & Combellick, R. (2003). *Seismic Microzonation: Metropolitan area of Anchorage*. Part A and B. Final Report prepared for Alaska Science and Technology Foundation, Geophysical Institute, University of Alaska Fairbanks, Fairbanks, AK.

- Biswas, N., Martirosyan, A., Dutta, U., Dravinski, M., & Papageorgiou, A. (2004). Investigation for seismic zonation of Anchorage. In Y. T. Chen, G. F. Panza, & Z. L. Wu (Eds.), *earthquake hazard, risk, and strong ground motion, IUGG Special Volume* (pp. 243–257). Seismological Press.
- Bonilla, L. F., Steidl, J. H., Lindley, G. T., Tumarkin, A. G., & Archuleta, R. J. (1997). Site amplification in the San Fernando Valley, California: Variability of site-effect estimation using the S-wave, coda, and H/V methods. *Bulletin of the Seismological Society of America*, 87(3), 710–730.
- Boore, D. (2013). ROSE School Engineering Seismology Lecture Notes: ROSE\_2013\_W2D3L1\_ground\_motions\_from\_simulations. [http://www.daveboore.com/short\\_course\\_lectures\\_and\\_labs.html](http://www.daveboore.com/short_course_lectures_and_labs.html). Accessed 17 May 2020.
- Brune, J. N. (1970). Tectonic stress and the spectra of seismic shear waves from earthquakes. *Journal of Geophysical Research*, 75(26), 4997–5009.
- Building Sciences Safety Council (BSSC). (2019). *BSSC Project Final Report: Development of the Next Generation of Seismic Design Value Maps for the 2020 NEHRP Provisions*. National Institute of Building Sciences.
- Castro, R. R., Pacor, F., Bindi, D., & Luzi, L. (2004). Site response of strong motion stations in the Umbria, Central Italy, Region. *Bulletin of the Seismological Society of America*, 94(2), 576–590. <https://doi.org/10.1785/0120030114>
- Census.gov. (2020). <https://www.census.gov/quickfacts/anchorage-municipality-alaska-county>. Accessed 23 Feb 2020.
- Combellick, R. A. (1999). Simplified geologic map and cross sections of central and east Anchorage, Alaska, Alaska Division of Geological & Geophysical Surveys Preliminary Interpretive Report 1999–1, p. 13, 2 sheets. <https://doi.org/10.14509/2243>.
- Douglas, J., & Boore, D. M. (2011). High-frequency filtering of strong-motion records. *Bulletin of Earthquake Engineering*, 9, 395–409. <https://doi.org/10.1007/s10518-010-9208-4>
- Dutta, U., Biswas, N., Martirosyan, A., Papageorgiou, A., & Kinoshita, S. (2003). Estimation of Earthquake Source Parameters and Site Response in Anchorage, Alaska from Strong-Motion Network Data Using Generalized Inversion Method. *Physics of the Earth and Planetary Interiors*, 137(2003), 13–29. [https://doi.org/10.1016/S0031-9201\(03\)00005-0](https://doi.org/10.1016/S0031-9201(03)00005-0)
- EERI. (2019). Webinar Recording: Anchorage, Alaska Reconnaissance Briefing, February 14, 2019, [http://www.learningfromearthquakes.org/2018-11-30-anchorage-alaska/index.php?option=com\\_content&view=article&id=68](http://www.learningfromearthquakes.org/2018-11-30-anchorage-alaska/index.php?option=com_content&view=article&id=68). Accessed 14 May 2020.
- Franke, K. W., Koehler, R. D., Beyzaei, C. Z., Cabas, A., Pierce, I., Stuedlein, A., & Yang, Z. (2019). Geotechnical engineering reconnaissance of the 30 November 2018 Mw 7.0 Anchorage, Alaska Earthquake, GEER Rept. GEER-059, Geotechnical Extreme Events Association, p. 1, <https://doi.org/10.18118/G6P07F>.
- Frey Mueller, J. T., Woodward, H., Cohen, S. C., Cross, R., Elliot, J., Larsen, C. F., Hreinsdóttir, S., & Zweck, C. (2008). Active deformation processes in Alaska, based on 15 years of GPS measurements. In J. T. Frey Mueller, P. J. Haeussler, R. L. Wesson, & G. Ekström (Eds.), *Active tectonics and seismic potential of Alaska: American Geophysical Union Geophysical Monograph Series 179* (pp. 1–42). Wiley.
- Glass, R. L. (1988). Map Showing Depth to Bedrock, Anchorage, Alaska. Open File Report 88–198, USGS. 1988. <https://doi.org/10.3133/ofr88198>.
- Goldstein, P., Dodge, D., Firpo, M., & Minner, L. (2003). SAC2000: Signal processing and analysis tools for seismologists and engineers. In W. H. K. Lee, H. Kanamori, P. C. Jennings, & C. Kisslinger (Eds.), *Invited contribution to The IASPEI International Handbook of Earthquake and Engineering Seismology*. Academic Press.
- Goldstein, P., & Snoko, A. (2005). *SAC Availability for the IRIS Community*. Incorporated Institutions for Seismology Data Management Center Electronic Newsletter.
- Goulet, C., Bozorgnia, Y., Abrahamson, N., Kuehn, N., Al Atik, L., Youngs, R., Graves, R., & Atkinson, G. (2018). Central and Eastern North America Ground-Motion Characterization, NGA-East Final Report, Pacific Earthquake Engineering Research Center, PEER Report No. 2018/08.
- Haessler, P. J., Best, T. C., & Waythomas, C. F. (2002). Paleoseismicity at high latitudes: Seismic disturbance of late Quaternary deposits along the Castle Mountain fault near Houston, Alaska. *Geological Society of America Bulletin*, 114, 1296–1310.
- Haeussler, P. J. (2008). An overview of the neotectonics of interior Alaska: Far-field deformation from the Yakutat microplate collision, in *Active Tectonics and Seismic Potential in Alaska*. In J. T. Freymueller, P. J. Haeussler, R. Wesson, & G. Ekström (Eds.), *Geophysics monograph series* (Vol. 179, pp. 83–108). American Geophysical Union. <https://doi.org/10.1029/179GM05>
- Hansen, W. R. (1965). Effects of the earthquake of March 27, 1964, at Anchorage, Alaska, U.S. Geol. Surv. Profess. Pap. (542-A), 68 pp.
- Havskov, J., & Ottemoller, L. (2010). *Routine data processing in earthquake seismology*. Springer. <https://doi.org/10.1007/978-90-481-8697-6>
- Hayes, G., Moore, G., Portner, D., Hearne, M., et al. (2018). 2018, Slab2, a comprehensive subduction zone geometry model. *Science*, 362, 58–61.
- Helffrich, G., Wookey, J., & Bastow, I. (2013). *The Seismic analysis code* (p. 2013). Cambridge University Press.
- Klin, P. (2019). GITANES (<https://www.mathworks.com/matlabcentral/fileexchange/61711-gitanes>), MATLAB Central File Exchange. Accessed 15 Aug 2019.
- Klin, P., Laurenzano, L., & Priolo, E. (2018). GITANES: A MATLAB package for joint estimation of site spectral amplification and seismic source spectra with the generalized inversion technique. *Seismological Research Letters*, 89(1), 182–190. <https://doi.org/10.1785/0220170080>
- Koehler, R. D., Farrell, R. E., Burns, P. A. C., & Combellick, R. A. (2012). Quaternary faults and folds in Alaska: A digital database, in Koehler, R.D., Quaternary Faults and Folds (QFF): Alaska Division of Geological & Geophysical Surveys Miscellaneous Publication 141, 31 p., 1 sheet, scale 1:3,700,000. <https://doi.org/10.14509/23944>.
- Laurenzano, G., Barnaba, C., Romano, M. A., et al. (2019). 2019, The Central Italy 2016–2017 seismic sequence: Site response analysis based on seismological data in the Arquata del Tronto-Montegallo municipalities. *Bulletin of Earthquake Engineering*, 17, 5449–5469. <https://doi.org/10.1007/s10518-018-0355-3>
- Liu, C., Lay, T., Xie, Z., & Xiong, X. (2019). Intraslab deformation in the 30 November 2018 Anchorage, Alaska, MW7.1 Earthquake. *Geophysical Research Letters*. <https://doi.org/10.1029/2019GL082041>
- Martirosyan, A., Dutta, U., Biswas, N., Papageorgiou, A., & Combellick, R. (2002). Determination of site response in



- Anchorage, Alaska, on the basis of spectral ratio methods. *Earthquake Spectra*, 18, 85–104.
- McNamara, D. E. (2000). Frequency dependent Lg attenuation in South-Central Alaska. *Geophysical Research Letters*, 27(23), 3949–3952.
- Oth, A., Parolai, S., Bindi, D., & Wenzel, F. (2009). Source spectra and site response from S waves of intermediate-depth Vrancea, Romania, Earthquakes. *Bulletin of the Seismological Society of America*, 99(1), 235–254. <https://doi.org/10.1785/0120080059>
- Parolai, S., Bindi, D., & Augliera, P. (2000). Application of the generalized inversion technique (GIT) to a microzonation study: Numerical simulations and comparison with different site-estimation techniques. *Bulletin of the Seismological Society of America*, 90(2), 286–297. <https://doi.org/10.1785/0119990041>
- Priolo, E., Pacor, F., Spallarossa, D., et al. (2019). Seismological analyses of the seismic microzonation of 138 municipalities damaged by the 2016–2017 seismic sequence in Central Italy. *Bulletin of Earthquake Engineering*, 18, 5553–5593. <https://doi.org/10.1007/s10518-019-00652-x>.
- Procella, R. L. (1979). Seismic Engineering Program Report, January–April 1979, Geologic Survey Circular 818-A, U.S. Department of the Interior, 1979.
- Ruppert, N., & Hansen, R. (2010). Temporal and spatial variations of local magnitudes in Alaska and Aleutians and comparison with body-wave and moment magnitudes. *Bulletin of the Seismological Society of America*, 100(3), 1174–1183. <https://doi.org/10.1785/0120090172>
- Schmoll, H. R., Barnwell, W. W. (1984). East-west geologic cross section along the DeBarr Line, Anchorage, Alaska: U.S. Geological Survey Open-File Report 84–791, 10 p., 1 sheet.
- Schmoll, H. R., Dobrovolsky, E. (1972). Generalized geologic map of Anchorage and vicinity, Alaska. US Geologic Survey Misc. Geol. Invest. Map I-787-D.
- Silwal, V., & Tape, C. (2016). Seismic moment tensors and estimated uncertainties in southern Alaska. *Journal of Geophysical Research: Solid Earth*, 121(4), 2772–2797. <https://doi.org/10.1002/2015JB012588>
- Souriau, A., Roullé, A., & Ponsolles, C. (2007). Site effects in the City of Lourdes, France, from H/V measurements: Implications for seismic-risk evaluation. *Bulletin of the Seismological Society of America*, 97(6), 2118–2136. <https://doi.org/10.1785/0120060224>
- Stachnik, J. C., Abers, G. A., & Christensen, D. H. (2004). Seismic attenuation and mantle wedge temperatures in the Alaska Subduction Zone. *Journal of Geophysical Research*, 109, B10304. <https://doi.org/10.1029/2004JB003018>
- Thornley, J., Dutta, U., Douglas, J., & Yang, Z. (2021a). Nonlinear site effects from the 30 November 2018 Anchorage, Alaska, Earthquake. *Bulletin of the Seismological Society of America*, 111, 2112–2120. <https://doi.org/10.1785/0120200347>
- Thornley, J., Dutta, U., Douglas, J., & Yang, Z. (2021b). Evaluation of horizontal to vertical spectral ratio and standard spectral ratio methods for mapping shear wave velocity across Anchorage, Alaska. *Soil Dynamics and Earthquake Engineering*. <https://doi.org/10.1016/j.soildyn.2021.106918>
- Thornley, J., Douglas, J., Dutta, U., & Yang, Z. (2021c). Site response spectral amplification ratios for Anchorage, Alaska Using Generalized Inversions of Strong-Motion Data (2004–2019). *PURE*. <https://doi.org/10.15129/217a8636-1cc3-400b-9f11-d86bc416f9e5>
- Thornley, J., Dutta, U., Fahringer, P., & Yang, Z. (2019). In situ shear-wave velocity measurements at the Delaney Park Down-hole Array, Anchorage. *Alaska. Seismological Research Letters*, 90(1), 395–400.
- U.S. Bureau of the Census. (1963). *U.S. Census of Population: 1960, Vol. I, characteristics of the population. Part 3, Alaska*. U.S. Government Printing Office.
- Ulery, C. A., & Updike, R. G. (1983). Subsurface structure of the cohesive facies of the Bootlegger Cove formation, southwest Anchorage: Alaska Division of Geological & Geophysical Surveys Professional Report 84, 5 p., 3 sheets, scale 1:15,840. <https://doi.org/10.14509/2257>.
- Updike, R. G., & Ulery, C. A. (1986). Engineering-Geologic Map of Southwest Anchorage, Alaska. Alaska Division of Geological and Geophysical Surveys Professional Report 89, sheet 1 of 1.
- Updike, R.G., Olsen, H.W., Schmoll, H.R., Kharaka, Y.K., & Stoke, K.H. (1988). Geologic and Geotechnical Conditions Adjacent to the Turnagain Heights Landslide, Anchorage, Alaska, U.S. Geological Survey Bulletin 1817, Department of the Interior, 1988.
- USGS.gov, 2020, <https://earthquake.usgs.gov/earthquakes/events/alaska1964/>. Accessed 30 May 2020.
- Wesson, R. L., Boyd, O. S., Mueller, C. S., Bufe, C. G., Frankel, A. D., Petersen, M. D. (2007). Revision of time-Independent probabilistic seismic hazard maps for Alaska: U.S. Geological Survey Open-File Report 2007–1043.
- West, M. E., Bender, A., Gardine, M., Gardine, L., Gately, K., Haeussler, P., Hassan, W., et al. (2020). The 30 november 2018 Mw 7.1 anchorage earthquake. *Seismological Research Letters*, 91(1), 66–84. <https://doi.org/10.1785/0220190176>
- Wilson, F. H., Hults, C. P., Schmoll, H. R., & Haeussler, P. J. (2012). Geologic map of the Cook Inlet region, Alaska, including parts of the Talkeetna, Talkeetna Mountains, Tyonek, Anchorage, Lake Clark, Kenai, Seward, Iliamna, Seldovia, Mount Katmai, and Afognak 1:250,000-scale quadrangles. Reston, VA, p. i-71. 2012. (3153).
- Xiong, F., & Yang, Z. (2008). Effects of seasonally frozen soil on the seismic behavior of bridges. *Cold Regions Science and Technology*, 54(2008), 44–53.
- Yang, Z., Dutta, U., Celebi, M., Liu, H., Biswas, N., Kono, T., & Benz, H. (2004). Strong-motion instrumentation and structural response at wood building in Downtown Anchorage, Alaska. In: 13th World Conference on Earthquake Engineering, Vancouver, B.C., Canada, August 1–6, 2004, Paper No. 1136.
- Zhu, C., Cotton, F., Kawase, H., Handel, A., Pilz, M., & Nakano, K. (2021). How well can we predict earthquake site response so far? Site-specific approaches. *ResearchGate Preprint*. <https://doi.org/10.13140/RG.2.2.14132.37762/1>